The SAMI Galaxy Survey: kinematics of dusty early-type galaxies

Bassett, R., Bekki, K., Cortese, L., Couch, W. J., Sansom, Anne E, van de Sande, J., Bryant, J. J., Foster, C., Croom, S. M., Brough, S., Sweet, S. M., Medling, A. M., Owers, M. S., Driver, S. P., Davies, L. J. M., Wong, O. I., Groves, B. A., Bland-Hawthorn, J., Richards, S. N., Goodwin, M., Konstantopoulos, I. S. and Lawrence, J. S.

Bassett, R., Bekki, K., Cortese, L., Couch, W. J., Sansom, Anne E ORCID: 0000-0002-2782-7388, van de Sande, J., Bryant, J. J., Foster, C., Croom, S. M. et al (2017) The SAMI Galaxy Survey: kinematics of dusty early-type galaxies. Monthly Notices of the Royal Astronomical Society, 470 (2). pp. 1991-2006. ISSN 0035-8711

Monthly Notices of the ROYAL ASTRONOMICAL SOCIETY
MNRAS **470**, 1991–2006 (2017) doi:10.1093/mnras/stx1000
Advance Access publication 2017 May 3

The SAMI Galaxy Survey: kinematics of dusty early-type galaxies

R. Bassett,[1★] K. Bekki,[1] L. Cortese,[1] W. J. Couch,[2] A. E. Sansom,[3] J. van de Sande,[4] J. J. Bryant,[2,4,5] C. Foster,[2] S. M. Croom,[4,5] S. Brough,[2] S. M. Sweet,[6] A. M. Medling,[6,7†] M. S. Owers,[2,8] S. P. Driver,[1] L. J. M. Davies,[1] O. I. Wong,[1,5] B. A. Groves,[6] J. Bland-Hawthorn,[4] S. N. Richards,[2,4,5] M. Goodwin,[2] I. S. Konstantopoulos[2,9] and J. S. Lawrence[2]

[1]*International Centre for Radio Astronomy Research, University of Western Australia, 7 Fairway, Crawley, WA 6009, Australia*
[2]*Australian Astronomical Observatory, PO Box 915, North Ryde, NSW 1670, Australia*
[3]*Jeremiah Horrocks Institute, University of Central Lancashire, Preston PR1 2HE, UK*
[4]*Sydney Institute for Astronomy, School of Physics, A28, The University of Sydney, NSW 2006, Australia*
[5]*ARC Centre of Excellence for All-sky Astrophysics (CAASTRO)*
[6]*Research School for Astronomy and Astrophysics, Australian National University, Canberra, ACT 2611, Australia*
[7]*Cahill Center for Astronomy and Astrophysics, California Institute of Technology, MS 249-17 Pasadena, CA 91125, USA*
[8]*Department of Physics and Astronomy, Macquarie University, NSW 2109, Sydney, Australia*
[9]*Envizi Suite 213, National Innovation Centre, Australian Technology Park, 4 Cornwallis Street, Eveleigh, NSW 2015, Australia*

Accepted 2017 April 21. Received 2017 April 14; in original form 2016 December 11

ABSTRACT

Recently, large samples of visually classified early-type galaxies (ETGs) containing dust have been identified using space-based infrared observations with the *Herschel Space Telescope*. The presence of large quantities of dust in massive ETGs is peculiar as X-ray haloes of these galaxies are expected to destroy dust in $\sim 10^7$ yr (or less). This has sparked a debate regarding the origin of the dust: Is it internally produced by asymptotic giant branch stars, or is it accreted externally through mergers? We examine the 2D stellar and ionized gas kinematics of dusty ETGs using integral field spectroscopy observations from the SAMI Galaxy Survey, and integrated star formation rates, stellar masses and dust masses from the GAMA survey. Only 8 per cent (4/49) of visually classified ETGs are kinematically consistent with being dispersion-supported systems. These 'dispersion-dominated galaxies' exhibit discrepancies between stellar and ionized gas kinematics, either offsets in the kinematic position angle or large differences in the rotational velocity, and are outliers in star formation rate at a fixed dust mass compared to normal star-forming galaxies. These properties are suggestive of recent merger activity. The remaining ∼90 per cent of dusty ETGs have low velocity dispersions and/or large circular velocities, typical of 'rotation-dominated galaxies'. These results, along with the general evidence of published works on X-ray emission in ETGs, suggest that they are unlikely to host hot, X-ray gas consistent with their low M_* when compared to dispersion-dominated galaxies. This means that dust will be long-lived and thus these galaxies do not require external scenarios for the origin of their dust content.

Key words: dust, extinction – galaxies: interactions – galaxies: kinematics and dynamics.

1 INTRODUCTION

The recent launch of the *Herschel Space Telescope* has made it possible for astronomers to study cold dust in a wide variety of galaxies with unprecedented sensitivity. As a consequence, a number of teams have identified large samples of visually classified early-type galaxies (ETGs) that clearly harbour massive reservoirs of cold dust (Cortese et al. 2012; Rowlands et al. 2012; Smith et al. 2012; Agius et al. 2013, 2015; di Serego Alighieri et al. 2013; Dariush et al. 2016). Although dust is closely related to the formation of stars in star-forming, late-type galaxies (LTGs), this may not be the case in ETGs where the level of ongoing star formation is typically much lower (if not non-existent). Furthermore, massive ETGs are known to contain large amounts of hot, X-ray-emitting gas that

★ E-mail: rbassett.astro@gmail.com
† Hubble Fellow.

is inhospitable to fragile dust grains. This hot gas rapidly destroys dust through a process known as thermal sputtering, resulting in a dust lifetime of $\sim 10^5$–10^7 yr (Draine & Salpeter 1979; Itoh 1989; Tsai & Mathews 1995; Mathews & Brighenti 2003; Clemens et al. 2010; Anderson et al. 2015).

The now undisputed presence of large quantities of dust in some ETGs has sparked a debate as to its origins. Many works have suggested that dust found in ETGs must have been recently accreted via mergers with gas-rich satellites (Goudfrooij & Trinchieri 1998; Kaviraj et al. 2009; Gomez et al. 2010; Davis et al. 2011; Shabala et al. 2012; Kaviraj et al. 2013; Davis et al. 2014; Dariush et al. 2016). In such a merger, the accreted dust will be embedded in a cold medium (either atomic or molecular gas) that can provide shielding from X-ray photons, resulting in a longer lifetime than for dust produced internally (Temi, Brighenti & Mathews 2007; Clemens et al. 2010; Dasyra et al. 2012; Finkelman et al. 2012). Alternatively, the dust may result from internal processes such as cooling of hot halo gas (Fabian et al. 1994; Bregman et al. 2005; Lagos et al. 2014) or production in asymptotic giant branch (AGB) stars (Knapp 1985; Knapp, Gunn & Wynn-Williams 1992; Athey et al. 2002; Matsuura et al. 2009; Nanni et al. 2013). Currently, there is no clear consensus regarding the internal versus external origins of dust in ETGs, and it is possible that both play some role with the balance between the two sources depending on the properties of individual galaxies (Rampazzo et al. 2005; Cappellari et al. 2011; Finkelman et al. 2012).

Much of the recent work on dusty ETGs is based on samples selected by visual morphology. In such cases, it is not clear how certain we can be that such galaxies host a hot, X-ray-emitting halo. The X-ray properties of ETGs vary considerably. This X-ray emission is less dominant in lower mass ETGs (e.g. Boroson, Kim & Fabbiano 2011), in (apparently) younger ETGs (Sansom, Hibbard & Schweizer 2000; Sansom et al. 2006) and in ETGs with higher star formation (Su et al. 2015). Environment is also thought to play a role (e.g. Mulchaey & Jeltema 2010). Clear evidence of diffuse X-ray emission is found in massive galaxy clusters as well as the most massive individual ETGs ($10^{10.8}$ $M_{\odot}$ and higher; e.g. Anderson et al. 2015) with X-ray luminosities (L_X) significantly larger than 10^{40} erg s^{-1}. For LTGs, Mineo, Gilfanov & Sunyaev (2012) find $L_X < 10^{40}$ erg s^{-1} corresponding roughly to the high L_X cut-off for X-ray binary stars (see Fabbiano 2006, for a review). Thus, for galaxies observed with $L_X < \sim 10^{40}$ erg s^{-1}, particularly those with recent star formation, X-ray emission can be attributed to the cumulative emission from supernova (SN) remnants and X-ray binaries.

Recent spectroscopic work has provided a connection between galaxy kinematics and X-ray properties. In particular, galaxies with stellar velocity dispersions (σ) larger than $\sim$150 km s^{-1} are often found to have X-ray luminosities in excess of 10^{40} erg s^{-1} (Boroson et al. 2011; Sarzi et al. 2013; Kim & Fabbiano 2015; Goulding et al. 2016), and these galaxies appear to extend the relationship between L_X and stellar mass found in massive galaxy clusters (e.g. Wu, Xue & Fang 1999; Ortiz-Gil et al. 2004; Zhang et al. 2011, and references therein) to lower mass systems. Below $\sigma = 150$ km s^{-1}, all ETGs studied by Goulding et al. (2016) have $L_X < 10^{40}$ erg s^{-1}, in the range attributed to X-ray binaries by Mineo et al. (2012). Furthermore, recent simulations by Negri et al. (2014b) have shown that galaxy rotation can also act to reduce L_X. This occurs because conservation of angular momentum in rotating galaxy models encourages the growth of cold gas discs, preventing large amounts of hot gas from collecting in the central region. These results suggest that kinematic observations of visually selected, dusty ETGs may distinguish galaxies embedded in a massive halo of hot gas from those more hospitable to long-lived dust reservoirs. It is also worth noting that visual morphology and kinematic classifications are not always well correlated (see Cappellari 2016, for a recent review of this topic).

This connection between X-ray-emitting gas content and kinematics shows that spatially resolved observations using integral field spectroscopy (IFS), which give a detailed description of a galaxy's kinematics, can help in understanding the origins of dust in ETGs. IFS observations of large samples of galaxies identified as dusty ETGs provide a step forward in two respects. First, because IFS allows global measurements of stellar σ covering most of the galaxy, they can clearly identify galaxies with large stellar σ that most likely host X-ray-emitting gas. Secondly, IFS observations provide a strong indicator of recent merger activity through the direct comparison of ionized gas and stellar kinematics. The work of Davis et al. (2011) using galaxies from the ATLAS^{3D} survey is an example in this vein, showing a connection between the detection of molecular gas in ETGs and misalignments between ionized gas and stellar kinematics. A scenario in which dust is produced internally is less likely to produce kinematic misalignments, particularly where dust originates directly from AGB stars. Galaxy mergers in simulations often produce misalignments (e.g. Balcells & Quinn 1990; Thakar et al. 1997; Bendo & Barnes 2000; Di Matteo et al. 2007; Bassett et al. 2017); thus, mergers represent a natural source for externally produced dust in ETGs.

In this work, we examine the origins of dust in ETGs using data from the SAMI Galaxy Survey (Bryant et al. 2015). The majority of Sydney-AAO Multi-object Integral field spectrograph (SAMI) galaxies are selected from the Galaxy And Mass Assembly survey (GAMA; Driver et al. 2011); therefore, we focus on the samples of dusty ETGs selected from GAMA by Agius et al. (2013, hereafter A13) and Agius et al. (2015, hereafter A15). We begin by considering those 540 GAMA galaxies observed by the SAMI survey that are found to have high-quality kinematic measurements (see Section 4) and clearly defined visual morphologies. We choose to explore the kinematics of A13/A15 galaxies rather than other samples of dusty ETGs (e.g. Rowlands et al. 2012; Dariush et al. 2016) as we find the largest overlap with this sample, which amounts to 49 *Herschel*-detected and 99 *Herschel*-non-detected galaxies. Together, Rowlands et al. (2012) and Dariush et al. (2016) have a total of four galaxies currently observed by SAMI.

This paper is structured as follows: In Sections 2 and 3, we present the samples and data sets considered. Section 4 presents our method of extracting integrated kinematic quantities from SAMI IFS observations as well as our kinematic criteria for isolating those visually classified dusty ETGs that are most likely to host hot X-ray-emitting gas. In Section 5, we apply this selection to those galaxies from A13/A15 observed by SAMI. In Section 6, we discuss the evolutionary implications of our results, and in Section 7, we summarize our conclusions. Throughout this work, we adopt a Λ cold dark matter cosmology with $\Omega_m = 0.3$, $\Omega_\Lambda = 0.7$ and $H_0 = 70$ km s^{-1} Mpc^{-1}.

2 SAMPLES

2.1 Dusty ETGs: A13 and A15

The parent sample of Herschel-ATLAS-detected (H-ATLAS; Eales et al. 2010) ETGs were first identified and analysed by A13. Briefly, H-ATLAS is a 550 deg^2 infrared (IR) survey using the PACS and SPIRE instruments (targeting 100–500 μm) on the *Herschel Space Observatory* with an expected detection of $\sim$250 000 galaxies. A13 began by investigating the H-ATLAS detections for a sample of galaxies identified as ETGs in the GAMA data set through visual classification (Kelvin et al. 2014, see also Section 3.1.2), with active galaxies excluded based on the prescription of Kauffmann et al. (2003). The sample of A13 is restricted to the redshift range $0.013 < z < 0.06$ and absolute r-band magnitudes brighter than $M_r = -17.4$ providing a volume-limited sample in the r band. They find an H-ATLAS detection rate of 29 per cent (220/771), i.e. 29 per cent of the visually classified ETGs in GAMA have IR detections greater than 5σ. Rigby et al. (2011) show that in the H-ATLAS science demonstration phase, their survey data have a catalogue number density completeness of > 80 per cent with the remaining 20 per cent missing due to noise and/or blending of sources. The completeness for A13/A15 galaxies should be similar to this. Among H-ATLAS-detected ETGs, there is a trend for the ratio of dust mass to stellar mass to increase for bluer $NUV - r$ colour, implying that recent star formation is likely associated with an increased presence of dust.

2.2 SAMI overlap with A13/A15

In this paper, we wish to explore the resolved kinematics of the sample of dusty ETGs presented in A13 and A15. While A13 includes dust masses for 220 dusty ETGs, only 49 of these have high-quality observations in the SAMI Galaxy Survey. Similarly, the study of A13/A15 includes 551 H-ATLAS-non-detected galaxies, of which 99 have high-quality SAMI survey observations. We expect the properties of those galaxies from A13/A15 that overlap with our SAMI observations to be fairly representative of the full sample of A13/A15 galaxies as the SAMI survey is selected to be representative of the GAMA survey, the parent sample of A13/A15.

It is important to know whether the A13/A15 galaxies for which we can investigate the resolved kinematics are representative of the original parent distribution. In Fig. 1, we show histograms of r-band magnitude, $\log_{10}(r_e)$ and $\log_{10}(M_*)$ comparing those galaxies from A13/A15 that have been observed with SAMI (in blue) with those that have not (in red). We then perform a two-sample Kolmogorov–Smirnov (KS) test for each of the three galaxy properties for these two subsamples. The resulting p-values of this are given in the top right-hand corner of each panel. The p-value indicates the percentage of the time we should expect to find the observed level of difference between the two samples, given their sizes, under the null hypothesis that they are randomly drawn from the same parent sample (typically, the null hypothesis is not rejected where the p-value is larger than 0.01). For r-band magnitude, r_e and M_*, we find p-values of 0.605, 0.312 and 0.642, meaning that we cannot reject the null hypothesis that these samples come from the same parent distribution. KS-test results for H-ATLAS-non-detected A13/A15 galaxies show less agreement in properties between the full sample and those observed with SAMI with p-values for r-band magnitude, r_e and M_* of 0.374, 0.075 and 0.132, respectively. Although we find slightly less agreement for non-detections, the p-values suggest that, again, we cannot reject the null hypothesis that those observed by SAMI are representative of the parent sample.

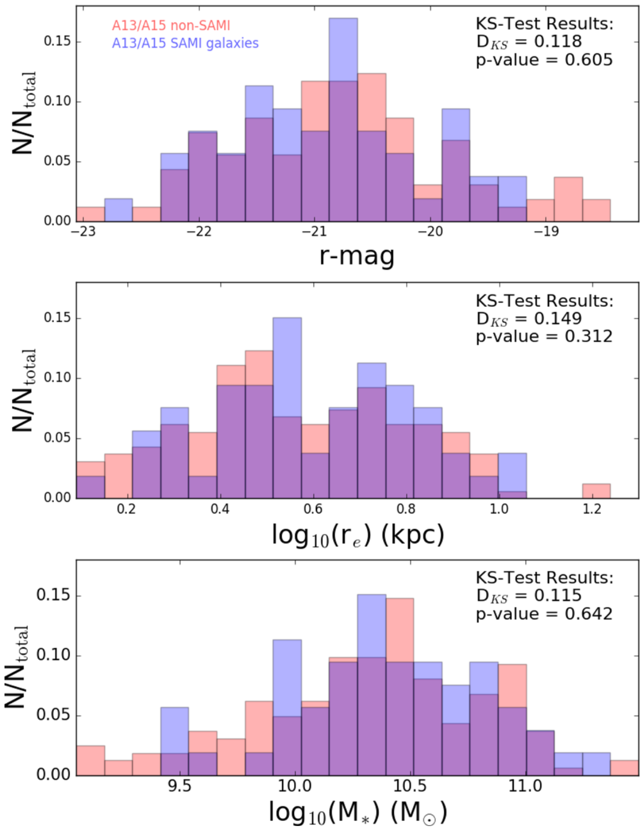

Figure 1. Histograms of r-band absolute magnitude, $\log_{10}(r_e)$ and $\log_{10}(M_*)$, comparing the full A13/A15 H-ATLAS-detected sample (red) with the subsample of these galaxies observed with SAMI (blue). For each galaxy property, we perform a two-sample KS-test and the results are indicated in the bottom right-hand corner of each panel. For each of the three properties considered here, the KS-test results show that we cannot reject the null hypothesis that these galaxies are selected from the same parent distribution.

3 DATA

3.1 SAMI survey data

Data analysed in this work come from the SAMI Galaxy Survey (Bryant et al. 2015), which aims to observe ~3600 galaxies using the SAMI integral field spectrograph (IFS; Croom et al. 2012) at the 3.9-m Anglo-Australian Telescope in the redshift range $0.004 < z < 0.095$. Observations using the SAMI IFS represent a step forward from more traditional IFS instruments due to the use of multiple fibre bundles (hexabundles; Bland-Hawthorn et al. 2011; Bryant et al. 2014) allowing for simultaneous observations of multiple galaxies with a roughly circular, ~14.7 arcsec diameter coverage. Fibres are fed into the AAOmega spectrograph (Sharp et al. 2006), which observes two spectral ranges using a red and blue arm set-up. This provides a coverage with 3700–5700 Å at resolution $R = 1812$ and with 6300–7400 Å at resolution $R = 4263$ (Croom et al. 2012; Bryant et al. 2015).

SAMI was designed to be representative of the highly complete (>98 per cent; Driver et al. 2011) GAMA survey rather than to complete itself due to observational constraints. As we have mentioned, H-ATLAS-detected A13/A15 galaxies should have a completeness of >80 per cent similar to the overall H-ATLAS survey. We have shown in Fig. 1 that H-ATLAS-detected A13/A15 galaxies with reliable SAMI kinematics are representative of the overall A13/A15 sample; thus, we do not expect completeness issues in the SAMI survey to affect our results.

At the time this paper was written, 1094 galaxies had been observed by the SAMI Galaxy Survey. Of these, 753 have had stellar kinematics measurements performed, as described in Section 3.1.1.

We then perform two quality cuts on this sample of 753 galaxies. First, we utilize only those galaxy observations that include enough high signal-to-noise ratio (S/N) spaxels such that we can measure the rotation curve beyond its turnover radius (see Section 4 for more information). Next, we remove galaxies that exhibit highly uncertain visual classifications of their morphologies (see Cortese et al. 2016). Our cut on stellar kinematics quality removes 199 galaxies, while the morphological cut removes a further 14 galaxies, resulting in a final sample of SAMI survey galaxies of 540. We use the kinematic measurements of this large sample of galaxies to determine if a given galaxy is supported by rotation or by random motions. We note that our stellar kinematic quality cut removes three H-ATLAS-detected galaxies from A13/A15 due to large stellar velocity dispersion errors, and our morphological quality cut removes a further one A13/A15 dusty ETG. All four of these galaxies, however, have relatively low velocity dispersions, thus excluding them does not affect our conclusions.

3.1.1 *Stellar and ionized gas kinematics*

Here we briefly describe the stellar kinematics fitting process; however, for a more detailed description, see Fogarty et al. (2015) and van de Sande et al. (in press). Stellar kinematics are measured using the penalized pixel-fitting (PPXF; Cappellari & Emsellem 2004) routine, which has become the standard method for use with IFS data cubes (e.g. Emsellem et al. 2007; Jimmy et al. 2013; Bassett et al. 2014; Ma et al. 2014). The PPXF method convolves spectral templates with a line-of-sight velocity distribution (LOSVD) parametrized using Gauss–Hermite polynomials. The first and second moments of this LOSVD provide the stellar velocity and velocity dispersion, respectively. In this work, we are concerned only with these first two moments; however, see van de Sande et al. (2017) for a detailed analysis of higher order moments.

Ionized gas kinematics for SAMI galaxies are measured from emission-line spectra using the LZIFU spectral fitting pipeline (Ho et al. 2016b). Prior to fitting, the best-fitting stellar continuum model from our PPXF procedure is subtracted from the spectra in each spaxel to provide more reliable fits. Gas velocities and velocity dispersions are then extracted from Gaussian fits to ionized gas emission lines. The LZIFU pipeline provides single Gaussian fits as well as more complex fits employing two and three Gaussian components. For the analysis presented in this paper, we are primarily interested in the circular velocity, V_c, and kinematic position angle (PA, both described in Section 4.3) for the primary component of the ionized gas. Therefore, we use the simple, single-component fits. For more detail on SAMI ionized gas kinematics fits, see Ho et al. (2014, 2016a,b).

3.1.2 *Galaxy morphology*

Galaxy morphologies had been determined through visual classification by an internal SAMI working group based on Sloan Digital Sky Survey (SDSS; York et al. 2000) Data Release 9 (DR9) red giant branch images for all SAMI galaxies observed at the time this paper was written. This classification, described in Cortese et al. (2016), is independent of, but similar to, the scheme of Kelvin et al. (2014) used by the GAMA survey. This involves a step-by-step procedure in which galaxies are first broadly classified as spheroid-dominated or disc-dominated, then placed into subclasses based on finer details. As SAMI galaxies in this work are selected from the GAMA survey, all galaxies here have been classified by both teams with three key differences. First, GAMA team members performed classifications on false colour *g*-, *i*- and *H*-band composite images, while SAMI team members utilize SDSS DR9 *gri* images. Secondly, the classification working groups from both surveys are composed of independent groups of classifiers who will each have their own unique classification bias. Thirdly, SAMI classifications include two criteria for identifying LTGs not used by Kelvin et al. (2014), namely, the presence of spiral arms and signs of star formation (based on colour rather than purely on morphology). Discussion of differences between the classifications of the two groups can be found in Section 6.1. As noted previously, 14 galaxies determined to be 'unclassified' (see Cortese et al. 2016) are excluded from our analysis, and only one of these comes from the A13/A15 samples. This galaxy, although it has an H-ATLAS detection, has a low velocity dispersion. Thus, excluding it does not affect our conclusions. For consistency with A13/A15, galaxies with elliptical, S0 and Sa visual classifications are defined as ETGs.

3.2 Stellar mass, dust mass and SFR

In Section 5.2, we explore the dust mass scaling relations of A13/A15 galaxies considered in this work. The GAMA survey provides a number of ancillary data products, which are available for all A13/A15 galaxies observed by SAMI. Briefly, the GAMA survey is a multiwavelength survey of hundreds of thousands of low-redshift galaxies. The core of the GAMA survey is a spectroscopic survey at optical wavelengths using the AAOmega instrument at the Anglo-Australian Telescope. This spectroscopic campaign is bolstered by data-sharing agreements and coordination with other independent imaging surveys covering the entire electromagnetic spectrum, from X-rays to radio. For more information on the goals, target selection and public data releases of GAMA survey data, see Driver et al. (2009, 2011), Baldry et al. (2010) and Liske et al. (2015).

Using data products from the GAMA survey, we explore stellar masses (M_*), dust masses (M_d) and star formation rates (SFRs) derived from full spectral energy distribution (SED) fits to ultraviolet (UV) to far-infrared (far-IR) observations using the MAGPHYS code based on the models of da Cunha, Charlot & Elbaz (2008). MAGPHYS has the distinct advantage over more traditional SED fitting techniques (e.g. Bruzual & Charlot 2003) as the inclusion of far-IR wavelengths allows for a direct balancing of energy from young, hot stars and warm/cold dust emission, resulting in more robust SFRs as well as estimates of M_d. Preliminary results from MAGPHYS-determined values for GAMA galaxies have been explored by Davies et al. (2016) and Driver et al. (2016), and full details of the MAGPHYS analysis will be presented in Driver et al. (2017).

Although all SAMI galaxies (including both H-ATLAS-detected and H-ATLAS-non-detected galaxies from A13/A15) have MAGPHYS estimates of M_d, estimates for H-ATLAS-non-detected galaxies are highly uncertain due to the lack of far-IR data. For this reason, we estimate upper limits to the dust masses for H-ATLAS-non-detected galaxies following the procedure of A13/A15. This procedure is described in Appendix A. Both M_* and SFR can more reliably be extracted in the absence of far-IR detections; thus, these values are taken from the GAMA survey for both H-ATLAS-detected and H-ATLAS-non-detected A13/A15 galaxies.

4 GLOBAL KINEMATICS AND KINEMATIC GALAXY SELECTION

Here we first describe our methods of extracting the global stellar kinematic quantities of rotational velocity, V_c, and flux-weighted velocity dispersion, $\sigma_{\rm mean}$, from our IFS observations. This is followed by a description of our method of selecting galaxies with stellar kinematics dominated by random motions.

4.1 Circular velocity: $V_{\rm c}$

The first step in determining the stellar $V_{\rm c}$ for each galaxy is to determine the kinematic PA based on the observed stellar velocity map. This is achieved using the code FIT_KINEMATIC_PA (see e.g. Cappellari et al. 2011) on the SAMI stellar velocity maps. This code determines the global kinematic PA following the method described in appendix C of Krajnović et al. (2006). Next, we use the measured stellar kinematic PA of each galaxy to extract the projected rotation curves along the kinematic major axis and, from this fit, estimate the value of $V_{\rm c}$ using a custom PYTHON code. We briefly outline this procedure here; however, a more detailed description is given in Appendix B.

To recover $V_{\rm c}$, we trace an artificial slit of width 1.5 arcsec across the velocity map at an angle given by the PA. The velocity as a function of position along the slit is fitted by a piecewise function made up of two constant-velocity sections separated by a sloped linear segment describing the central velocity gradient. This functional form, which follows Epinat et al. (2009), provides two parameters: the turnover radius, $r_{\rm t}$, and $V_{\rm c}$. The latter is given by the constant velocity value beyond $r_{\rm t}$. For some observations, the coverage of the SAMI bundle does not extend beyond $r_{\rm t}$; thus, measured values of $V_{\rm c}$ are largely unconstrained. This is true for 199 of the 753 galaxies tested (including three H-ATLAS detected A13/A15 galaxies), and these galaxies are excluded from further analysis. Finally, we apply an inclination correction to $V_{\rm c}$ based on measured ellipticities and bulge-to-total ratios (B/T) taken from the GAMA survey and from Simard et al. (2011), respectively (our inclination correction is described fully in Appendix B).

4.2 Flux-weighted velocity dispersion: $\sigma_{\rm mean}$

We adopt the value $\sigma_{\rm mean}$, the flux-weighted stellar velocity dispersion, for our global velocity dispersion measure following previous IFS studies at various redshifts (Epinat et al. 2009; Law et al. 2009; Jones et al. 2010; Wisnioski et al. 2011; Green et al. 2014). Prior to measuring the stellar $\sigma_{\rm mean}$, we mask spaxels with large uncertainties on σ following the procedure of van de Sande et al. (2017). $\sigma_{\rm mean}$ is then defined as

$$\sigma_{\rm mean} = \frac{\sum_i \sum_j F(i, j) \times \sigma(i, j)}{\sum_i \sum_j F(i, j)}, \qquad (1)$$

where $F(i, j)$ is the flux observed in the spaxel with i and j as its spatial position, and $\sigma(i, j)$ is the corresponding stellar velocity dispersion. We find that this measurement is robust for all galaxies with SAMI coverage beyond $r_{\rm t}$, as described in Section 4.1. A rough correction for the effects of beam smearing is applied following Bassett et al. (2014), where the artificial σ induced by the seeing is subtracted from $\sigma_{\rm mean}$ in quadrature. For a detailed description of our masking and beam-smearing correction procedure, see Appendix C. For simplicity, all remaining references to $V_{\rm c}$ and $\sigma_{\rm mean}$ in this paper refer specifically to inclination-corrected and beam-smearing-corrected values, respectively.

4.3 Kinematic galaxy selection

In this section, we utilize galaxy stellar kinematics from IFS observations to select dispersion-dominated galaxies (DDG) in a less ambiguous way than visual morphological classification. We would like to know how many galaxies that are visually classified as ETGs are really dispersion-dominated systems, and how many have kinematic properties more similar to rotationally supported LTGs. The latter are typified by S0 galaxies, which, by definition, exhibit a significant disc component.

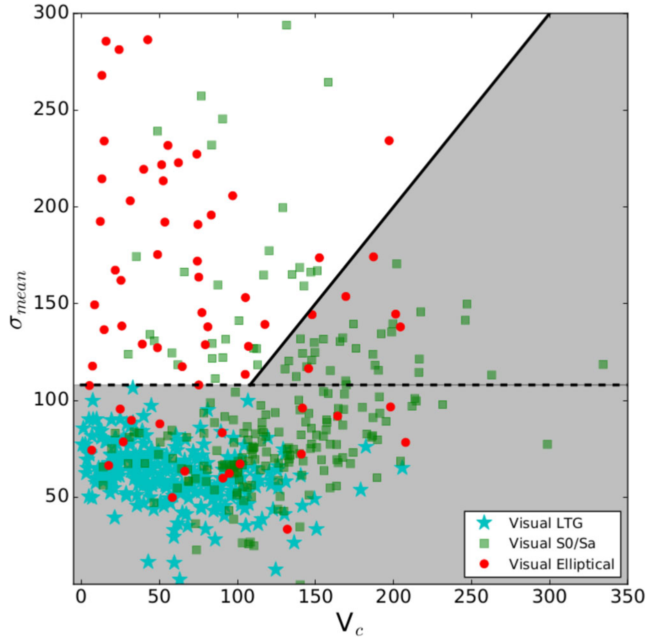

Figure 2. A depiction of our kinematic classification scheme based on $\sigma_{\rm mean}$ versus $V_{\rm c}$. We compare $V_{\rm c}$ versus $\sigma_{\rm mean}$ for three subsets in visual morphology: galaxies classified as elliptical by both SAMI and GAMA groups in (red circles), galaxies classified by both groups as later than Sa (blue stars), and galaxies classified as S0 or Sa by the SAMI team (green squares). The solid black line shows the one-to-one relation, and the black dashed line shows our $\sigma_{\rm mean}$ cut-off isolating visual LTGs. The black solid and black dashed lines are used to separate our three kinematic selections.

Our stellar kinematic selection is depicted in Fig. 2, where we plot $\sigma_{\rm mean}$ versus $V_{\rm c}$. Plotted symbols indicate different visual morphologies taken from our SAMI classifications. We note that the velocity resolution of the SAMI survey is 70 km s^{-1}, which means that many of our low stellar $\sigma_{\rm mean}$ values will be upper limits. In particular, this will be the case for a very large fraction of visually classified LTGs at low $V_{\rm c}$, as this low measurement of $V_{\rm c}$ often results from a nearly face-on inclination. Measurements for face-on galaxies should provide a lower value of σ when compared to an edge-on view of the same object due to a minimal contribution from rotation and beam smearing. In their IFS study of face-on LTGs from the DiskMass Survey, Martinsson et al. (2013) find that 77 per cent (23/30) have line-of-sight stellar σ less than 70 km s^{-1} with an average value of 56.8 km s^{-1} for their entire sample. Thus, we should expect that low-$V_{\rm c}$ (more face-on on average) galaxies have $\sigma_{\rm mean}$ clustered near our σ resolution limit. We also note that we apply a larger beam-smearing correction for galaxies with a large $V_{\rm c}$ (see Appendix C), and the uncorrected measurements of $\sigma_{\rm mean}$ for these galaxies are up to 30 km s^{-1} larger than pictured in Fig. 2.

Visually classified ETGs (elliptical, S0 and Sa galaxies) are found to exhibit a large amount of scatter in $\sigma_{\rm mean}$ in Fig. 2, highlighting the pitfalls of assuming a one-to-one correspondence between visual morphology and kinematics; for example, visually classified ETGs have a large stellar velocity dispersion. Visually classified LTGs, on the other hand, are found to be more clustered. This is due to the fact that they are easier to identify from the presence of clear spiral arms, resulting in a much cleaner selection. S0/Sa galaxies, in general, extend the high-V_c end of the LTG distribution to higher $\sigma_{\rm mean}$. This is consistent with the result of Williams, Bureau & Cappellari (2010), who show that S0 galaxies exhibit a larger V_c than LTGs at fixed M_*.

Following the LTGs, we produce a selection to separate galaxies having kinematic properties consistent with those of visually selected LTGs. We initially perform a linear fit to the visual LTGs in Fig. 2, finding a slope of $-0.04\pm.04$. As this is consistent within errors to a flat slope, we simply employ a flat cut in $\sigma_{\rm mean}$, matching the cut-off value to the highest value observed for a visually selected LTG of 108.0 km s^{-1}. This cut is shown in Fig. 2 by the horizontal, black dashed line. By design, this isolates 100 per cent of LTGs in our sample; however, 31 per cent of visually classified elliptical galaxies also fall below this line (20/65).

We are interested in galaxies for which a large fraction of the dynamical support comes from random motions, implying a large $\sigma_{\rm mean}$ relative to V_c. For this reason, we also plot in both panels the one-to-one relation as a solid black line. Galaxies falling above this line have $\sigma_{\rm mean} > V_c$; thus, they are the most likely to derive a majority of their support from random motions (e.g. Weiner et al. 2006; Law et al. 2009; Lemoine-Busserolle & Lamareille 2010; Newman et al. 2012). We define galaxies falling above both this line and the black dashed line as 'dispersion-dominated' galaxies. The remaining galaxies we define as 'rotation-dominated' galaxies (RDGs). Comparing this kinematic selection with our sample of 540 SAMI galaxies with reliable kinematics, we find that 100 per cent of DDGs and 39 per cent (181/469) of RDGs are visually classified as ETGs. We reiterate the point from Section 3.1.2 that our definition of ETG includes Sa galaxies, however. If we redefine ETGs more strictly as only galaxies with visual classifications earlier than Sa, we find that 93 per cent (66/71) of DDGs and 14 per cent (66/469) of RDGs are considered ETGs.

Before moving on, we examine the relationship between the galaxy spin parameter, λ_R, and ellipticity, ϵ, for A13/A15 galaxies. Here, λ_R is calculated from our SAMI stellar kinematics maps as

$$\lambda_R = \frac{\sum_{k=1}^{n} F_k R_k |V_k|}{\sum_{k=1}^{n} F_k R_k \sqrt{V_k^2 + \sigma_k^2}}, \tag{2}$$

where F_k is the flux in spaxel k, and V_k and σ_k are the line-of-sight velocity and LOSVD in spaxel k. The value R_k is the semimajor axis of the ellipse defined by the r-band axis ratio (b/a) on which spaxel k lies (i.e. the intrinsic radius). This sum is performed using only spaxels within an ellipse defined by the galaxy effective radius, r_e, and b/a. For ATLAS$^{\rm 3D}$ galaxies, Emsellem et al. (2011) show that these parameters are useful in separating fast and slow rotators among their sample of ETGs. λ_R versus ϵ for our sample is shown in Fig. 3, where we plot RDGs, DDGs and H-ATLAS-detected ETGs from A13/A15. The dashed line shows the separation between slow versus fast rotators taken from Emsellem et al. (2011).

We find that there is a correspondence between λ_R versus ϵ and our kinematic selection, with a majority of DDGs falling at low λ_R and ϵ. This suggests that the two methods are tracing similar properties of SAMI galaxies, particularly in light of the large uncertainty in λ_R for SAMI observations (which, in some cases, is >0.4). Considering only H-ATLAS-detected ETGs from A13/A15, we find that employing the slow- versus fast-rotator selection of Emsellem et al. (2011) would retain only two galaxies, with one having significant rotation and a relatively large ϵ. We are able to double our sample of H-ATLAS-detected ETGs by employing the kinematic selection outlined here. We stress that, within uncertainties in our kinematic measurements, our kinematic selection and that of Emsellem et al. (2011) are tracing roughly the same population. In this work, however, we are primarily interested in galaxies with a large stellar velocity dispersion, which can be used as an indication of the presence of a hot, X-ray-emitting halo (e.g. Boroson et al. 2011; Sarzi et al. 2013; Goulding et al. 2016).

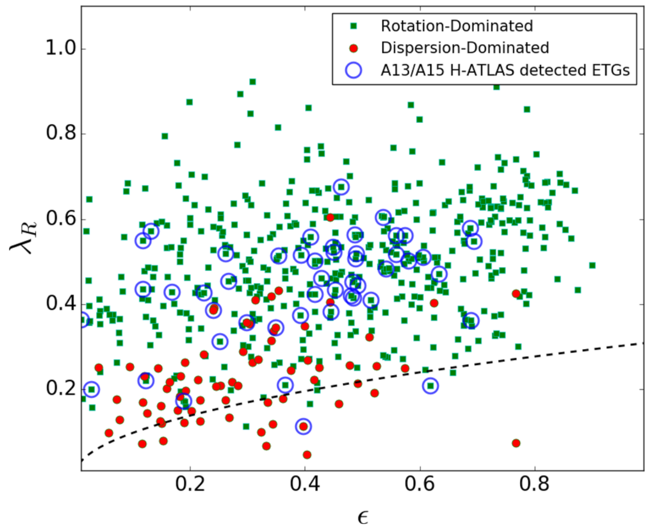

Figure 3. λ_R versus ϵ for SAMI galaxies, with A13/A15 H-ATLAS detections highlighted. Here we show SAMI RDGs and DDGs with cyan and green squares, respectively. The separation between slow and fast rotators from Emsellem et al. (2011) for ATLAS$^{\rm 3D}$ galaxies is shown with a black dashed line. We find that only two H-ATLAS detections are slow rotators and one exhibits rapid rotation based on our kinematic selection.

Although stellar σ is often used as a proxy for M_* (e.g. Faber & Jackson 1976), it has been shown that even massive, X-ray halo-hosting galaxies can host discs of cold gas and dust when rotating rapidly (Negri, Ciotti & Pellegrini 2014a; Negri et al. 2014b). Using our kinematic quantities, however, we can identify those galaxies likely to host hot X-ray-emitting gas, and further select only those low-rotation galaxies in which the presence of this gas would hinder the formation of long-lived dust grains. Figs 2 and 3 show that this may not be accomplished considering λ_R versus ϵ or by using M_* alone as an indicator of a hot interstellar medium (ISM).

5 RESULTS

5.1 Kinematics of A13/A15 galaxies

Having developed a stellar kinematic selection, we now apply this to those A13/A15 galaxies that have been observed by the SAMI Galaxy Survey. The V_c versus σ_m parameter space used to perform our kinematic selection is depicted in Fig. 4 for A13/A15 galaxies observed by SAMI with H-ATLAS non-detections shown by small cyan circles and H-ATLAS-detected galaxies shown by larger red circles. We also indicate galaxies having kinematic irregularities (described below) by green squares and blue pentagons.

From Fig. 4, it can be seen that a far larger fraction of DDGs are non-detections in the H-ATLAS survey. Indeed, considering all DDGs from A13/A15, 11 per cent (4/35) are H-ATLAS detections compared with 40 per cent (45/113) of RDGs. The entire

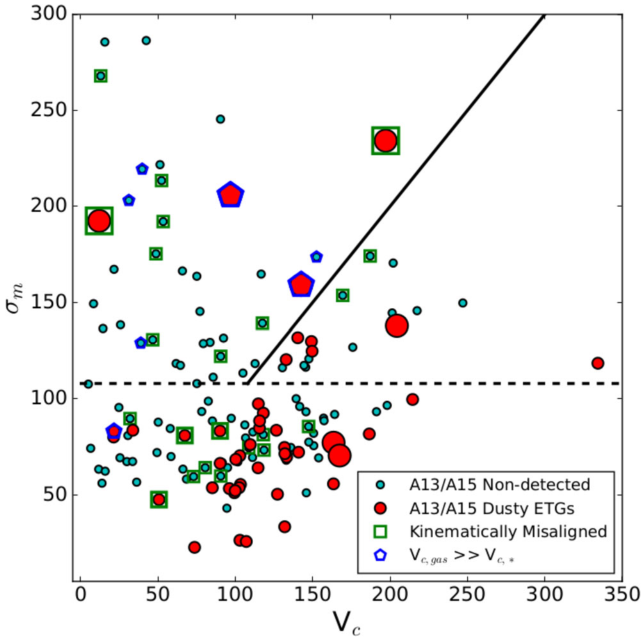

Figure 4. Stellar V_c versus σ_{mean} for H-ATLAS-detected and H-ATLAS-non-detected ETGs from A13/A15. H-ATLAS-non-detected galaxies are shown by the smaller cyan circles, while H-ATLAS-detected galaxies are indicated by the larger red circles. Red circles that are plotted with significantly larger symbols show those galaxies with $\log_{10}(M_*) > 10.8$, which are most likely to host a hot X-ray halo (see Section 5.2). Note, however, that some H-ATLAS-non-detected galaxies have $\log_{10}(M_*) > 10.8$, but these are not plotted with larger symbols. We also show kinematically misaligned galaxies with green squares, and galaxies for which the ionized gas rotation is significantly larger than that of the stars with blue pentagons.

sample of A13/A15 represents 771 galaxies, with 220 of these being H-ATLAS detections, or 29 per cent. This clearly shows that, although a low fraction of visually classified galaxies host appreciable amounts of dust, it is far more likely for galaxies with kinematics dominated by rotation. In the following sections, we examine more closely the kinematics of H-ATLAS-detected and H-ATLAS-non-detected galaxies from A13/A15.

5.1.1 Kinematics of H-ATLAS-detected ETGs

As mentioned in Section 2.2, only 49 of the 220 H-ATLAS-detected ETGs of A13/A15 have kinematics maps from the SAMI survey that meet our quality cuts, and this subset is shown in our σ_{mean} versus V_c diagram in Fig. 4 with red circles. We find that 45/49 (90 per cent) are RDGs, with 35 of these 45 having $V_c > 100$ km s^{-1}. This means that these galaxies derive a majority of their dynamical support from rotation as expected for LTGs, particularly for S0/Sa galaxies (as shown in Fig. 2). Galaxies such as these may host an X-ray-emitting halo if they are massive enough (e.g. Anderson et al. 2015); however, Negri et al. (2014a,b) have shown that rapid rotation can allow a galaxy to host a cold gas disc even in the presence of such a hot halo. Therefore, the presence of dust in these systems *does not* require an external origin scenario such as galaxy mergers.

Next, we investigate kinematics in our sample of four H-ATLAS-detected DDGs. A comparison between kinematics of the gas and stars for these four galaxies can be seen in Fig. 5, alongside their SAMI stellar and ionized gas kinematics and their H α flux maps. All four galaxies exhibit discrepancies between their stellar and ionized gas kinematics, indicating that the dust in these galaxies is related to significant accretion events, such as galaxy mergers, in their evolutionary histories. Here we identify two classes of 'kinematically irregular' galaxies, described in the following.

The first class of kinematically irregular galaxies are those with significant misalignments between the kinematic PAs of the stars and ionized gas. These galaxies have been identified by Bryant et al. (in preparation), and here we define kinematic misalignments as those galaxies with differences between the stellar and kinematic PA of $>30°$. Kinematically misaligned galaxies such as these show the clearest evidence from SAMI observations of having undergone a stochastic event, such as gas accretion, in the relatively recent past (similar to non-SAMI works; e.g. Knapp et al. 1989; McDermid et al. 2006; Davis et al. 2011, 2015; van de Voort et al. 2015). Bryant et al. (in preparation) find that the cut in stellar versus gas PA of 30° may not always provide an accurate descriptor of the fraction of misaligned galaxies due to observational issues (e.g. the depth of the data; see Bryant et al., in preparation); however, this will not affect our conclusions as kinematically misaligned galaxies included in our H-ATLAS-detected DDG sample have misalignments close to 90°. Such a large difference between stellar and gas kinematics gives the clearest indication of recent accretion.

Galaxies 551505 and 534655 fall into this first class, with both exhibiting kinematic misalignments of ∼90°. The two cases are not identical, however. Galaxy 551505 displays rapid rotation in both stars and ionized gas measured to the edge of the SAMI fibre bundle, which may suggest that this is a polar ring galaxy, a relatively stable configuration resulting from merger activity (Bekki 1998; Iodice et al. 2015, Bryant et al., in preparation). Galaxy 534655, on the other hand, exhibits very slow stellar rotation with a rapidly rotating ionized gas component in the central region, possibly indicative of a nuclear starburst. From preliminary analysis of emission-line ratios in the central region of this galaxy, we find possible evidence of a low-ionization nuclear emission-line-like emission (Medling et al., in preparation), consistent with this picture. Nuclear starburst activity such as this has also been linked to merger activity in local luminous IR galaxies (Sanders, Surace & Ishida 1999; Bekki & Shioya 2000; Hopkins et al. 2006; Haan et al. 2013).

In addition to kinematically misaligned galaxies, we also identify a second class of galaxies in which the stars and gas are kinematically aligned but have a significantly larger gas V_c when compared to that of the stars. In order for a galaxy to be included in this classification, we require the ratio of stellar to gas rotation, $V_{c,star}/V_{c,gas}$, to be <0.6, noting that values observed in LTGs as a result of asymmetric drift (a phenomenon related to the aging of stellar populations; Gomez & Mennessier 1977; Westfall et al. 2007) fall in the range ∼0.75–0.9 (Martinsson et al. 2013; Cortese et al. 2014, 2016). If the origin of the ionized gas content of an ETG were closely related to the existing stellar component, we would expect the two to share similar kinematics, unlike what we see in such cases. This implies that $V_{c,star}/V_{c,gas} < 0.6$ galaxies have experienced an accretion event in the past related to their gas and dust content, but the difference between the time this occurred and the time at which we observe the galaxy may be significantly longer than for kinematically misaligned galaxies, depending on the dynamical relaxation time of the system. Estimates of the relaxation time of gas discs in merger remnants range from ≪1 Gyr to ∼5 Gyr (Lake & Norman 1983; Davis & Bureau 2016); however, see Bryant et al. (in preparation) for a discussion of dynamical relaxation time in SAMI survey galaxies.

The other two galaxies in Fig. 5, 508180 and 511892, fall into our second class of kinematic irregularities. As noted, the typical values of $V_{c,star}/V_{c,gas}$ seen in LTGs due to asymmetric drift are

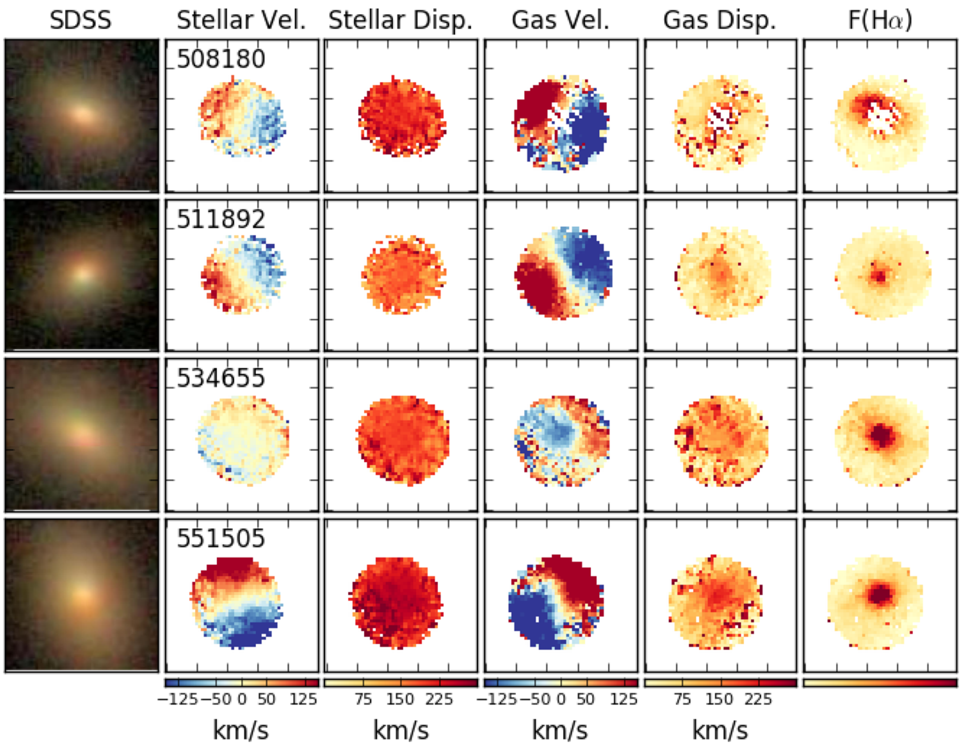

Figure 5. A montage showing morphologies and stellar and gas kinematics for the four H-ATLAS-detected galaxies from A13/A15 identified as DDGs from SAMI IFS observations. From the left- to right-hand side: SDSS *gri* image, stellar velocity map, stellar σ map, ionized gas velocity map, ionized gas σ map and H α flux map. The size of the SDSS image is matched to that of the SAMI kinematics maps at 25.0×25.0 arcsec^2. Columns 2–6 are derived from SAMI survey observations. The GAMA CATIDs of each galaxy are indicated above the stellar velocity maps. Colour bars for kinematics maps are in km s^{-1}, while, for a given galaxy, H α flux maps are displayed with a flux scale ranging from zero to three times the standard deviation of H α flux for that galaxy. Note that galaxy 508180 exhibits relatively weak Balmer emission in the central regions and poorly fitted Balmer absorption, resulting in the missing pixels for gas measurements of this galaxy.

~0.75–0.89, whereas in galaxies 508180 and 511892, this value is roughly half that at 0.35 and 0.49, respectively. One scenario would be a prograde minor merger where gas is accreted with a similar angular momentum to the accreting galaxy. Retrograde merger remnants are more likely to exhibit gas-stellar counter rotation after dynamical relaxation, particularly in cases where the primary galaxy is gas-poor prior to the merger (e.g. Bassett et al. 2017).

Of the 45 H-ATLAS-detected RDGs, four also show kinematic discrepancies similar to the four dusty DDGs. This is reasonable as minor mergers are not limited to massive, dispersion-supported galaxies. It is important to note that, although the dust content of some fraction of low-dispersion galaxies will indeed be related to accretion processes, these processes are not a necessity to account for the observed dust in the absence of a hot, X-ray halo. We also indicate with large symbols the H-ATLAS-detected ETGs with $\log_{10}(M_*) > 10.8$, which Anderson et al. (2015) find is the limiting mass above which galaxies show clear evidence for an X-ray-emitting ISM (see Section 5.2). Three RDGs fall in this category; however, they all have $V_c > 160$ km s^{-1}. Negri et al. (2014a,b) show in simulations that, even in the presence of an X-ray halo, rapid rotation can allow for the presence of a cold gas disc. Furthermore, two of these massive RDGs have $\sigma_{\rm mean} \simeq 75$ km s^{-1}, suggesting that these two galaxies do not follow the Faber–Jackson relation for massive ETGs (Faber & Jackson 1976). This discrepancy between their large M_* with a low $\sigma_{\rm mean}$ clearly illustrates that these galaxies must derive a significant amount of support from rotation.

5.1.2 *Kinematics of H-ATLAS-non-detected ETGs*

In this section, we briefly discuss the integrated kinematics of H-ATLAS non-detections from A13/A15. These galaxies are indicated in Fig. 4 as small cyan circles. Similar to H-ATLAS-detected ETGs, we find that non-detected galaxies also occupy the full range in $\sigma_{\rm mean}$ versus V_c as the 540 SAMI galaxies with reliable measurements, including a significant number of RDGs. We do find, however, that a larger percentage of non-detected galaxies fall in our DDG kinematic selection at 31 per cent (31/99) compared to 8 per cent (4/49) for H-ATLAS detections.

Next, we examine the level of kinematic irregularity among our 31 H-ATLAS-non-detected DDGs. As discussed in the previous section, kinematically irregular galaxies are thus defined based on a comparison of their stellar and ionized gas kinematics. While all 4 of our H-ATLAS-detected DDGs have strong ionized gas emission, only 35 per cent (11/31) of H-ATLAS-non-detected DDGs have ionized gas emission with a high enough S/N to evaluate this. Thus, a majority (20/31) of H-ATLAS-non-detected DDGs in our sample are poor in gas as well as dust, as is typical of low-redshift ETGs. Among the H-ATLAS-non-detected DDGs with ionized gas emission strong enough to measure rotation, 7/11 have kinematically misaligned gas and 4/11 exhibit $V_{\rm c,star}/V_{\rm c,gas} < 0.6$ (specifically 0.09, 0.10, 0.27 and 0.56). This is similar to kinematic irregularities seen in H-ATLAS-detected DDGs; therefore, the presence of dust does not impact the relative dynamics of gas compared to stars in ETGs with significant gas. We note, however, that the presence of ionized gas in the absence of a secure detection of dust emission is

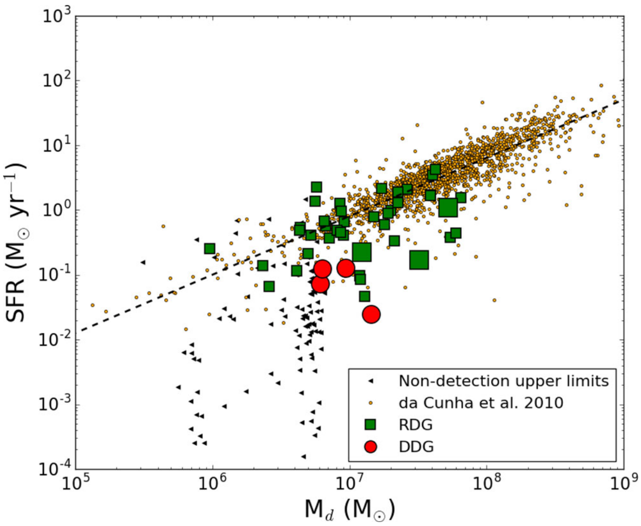

Figure 6. The relationship between M_d and SFR for dust ETGs of A13/A15 that have been observed by SAMI in comparison with normal $z = 0$ star-forming galaxies from da Cunha et al. (2010). Larger symbols indicate galaxies with $\log_{10}(M_*) > 10.8$, which are most likely to host a hot X-ray halo (note that all DDGs here fall into this selection). Upper limits for *Herschel*-non-detected galaxies from A13/A15 are also indicated with black triangles. Normal star-forming SDSS galaxies from da Cunha et al. (2010) follow a tight relationship between M_d and SFR, and the linear fit to these data points is shown by the dashed black line. A majority of RDGs follow this relation while DDGs fall below, having low SFR for their dust content when compared with normal SFR galaxies.

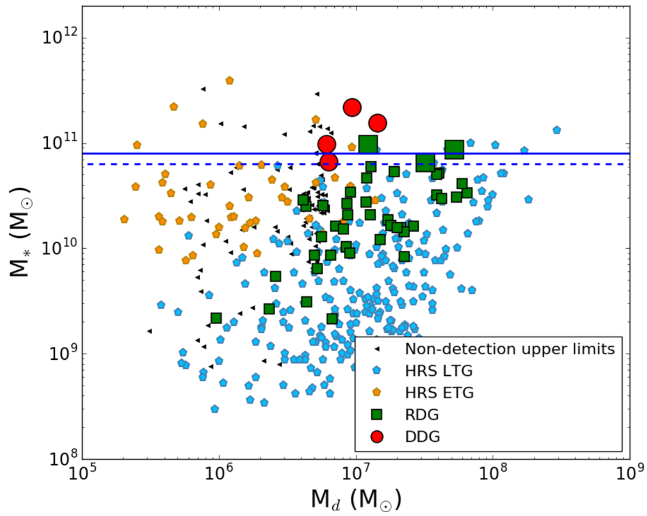

Figure 7. M_d versus M_* for SAMI-observed A13/A15 galaxies (symbols match those in Fig. 6), as well as very nearby galaxies from the HRS (Boselli et al. 2010). Blue and orange pentagons indicate HRS LTGs and HRS ETGs, respectively. We also show with horizontal blue lines the mass limit above which all elliptical galaxies from Anderson et al. (2015) show evidence of an extended X-ray-emitting halo.

not inconsistent with the presence of a hot, X-ray-emitting ISM in massive ETGs. We discuss this point further in Section 6.2.

For completeness, we note that among the full sample of DDGs in our SAMI kinematics sample, 58 per cent (41/71) have a high ionized gas emission with a high enough S/N to measure rotation. Among this subsample, 22/41 exhibit kinematic misalignments, while 13/41 fall in the $V_\mathrm{c,star}/V_\mathrm{c,gas} < 0.6$ class. Given our small sample size, our finding that 54 per cent of DDGs in our sample with appreciable amounts of ionized gas are kinematically misaligned agrees well with the work of Bryant et al. (in preparation). The authors find that, depending on the exact definitions, ∼40–53 per cent of ETGs from the full SAMI survey with high-S/N ionized gas emission are kinematically misaligned.

5.2 Dust properties of H-ATLAS-detected ETGs

Having shown that a majority of the visually classified dusty, ETGs from A13/A15 are consistent with being rotationally supported, we now investigate the dust content of our sample. Any differences between members of our kinematic selections (or lack thereof) may help to further identify the most likely origin scenario for their dust content. We present in Figs 6 and 7 the M_d–SFR and M_d–M_s relationships for our sample, with markers indicating our kinematic V_c–σ_mean selection. We also include upper limits on M_d for H-ATLAS non-detections from A13/A15 as small black triangles.

In Fig. 6, our observations of SFR versus M_d for A13/A15 galaxies are plotted over a large sample of 'normal' star-forming SDSS galaxies taken from da Cunha et al. (2010), which represent the $z = 0$ star-forming main sequence, plotted as small orange dots. Also plotted in Fig. 6 is a linear fit to M_d versus SFR from da Cunha et al. (2010), given by the black dashed line.

In Fig. 7, M_* versus M_d for A13/A15 galaxies is plotted over galaxies from the Herschel Reference Survey (HRS; Boselli et al. 2010; Cortese et al. 2012), representing a wide range of galaxy types and environments. Visually classified LTGs from the HRS are given by light blue pentagons, while orange pentagons show ETGs. Visual classifications for HRS galaxies are more reliable than those of SAMI galaxies because HRS galaxies are extremely nearby objects. The relative proximity of HRS galaxies also means that they are sensitive to much lower levels of total M_d than A13/A15, which is reflected in Fig. 7, where HRS ETGs overlap with A13/A15 upper limits. This selection effect, however, will not affect our conclusions. We also plot in Fig. 7 blue horizontal lines that correspond to stellar masses of galaxies from Anderson et al. (2015) that show evidence of an extended X-ray-emitting halo. The solid blue line is located at $\log_{10}(M_*/\mathrm{M}_\odot) = 10.9$, above which all galaxies show clear evidence of such a halo. Considering tentative detections, this can be extended to $\log_{10}(M_*/\mathrm{M}_\odot) = 10.8$, indicated by the dashed blue line. Anderson et al. (2015) explore the relationship between X-ray luminosity (L_X) and individual galaxy masses of $\log_{10}(M_*/\mathrm{M}_\odot) = 10.0$ using stacking of X-ray observations. Below $\log_{10}(M_*/\mathrm{M}_\odot) = 10.8$, they find no dependence between L_X and M_*, suggesting that the observed L_X can be explained by SN remnants and X-ray binaries rather than a hot gas halo. The results of Anderson et al. (2015) suggest that an alternative to using kinematics to select galaxies hosting X-ray gas haloes is to employ a fixed stellar mass limit of $\log_{10}(M_*/\mathrm{M}_\odot) = 10.8$.

Fig. 6 shows that DDGs are found to host a lower SFR at fixed M_d when compared to the bulk of RDGs; this difference is even greater when comparing to SDSS star-forming galaxies (a linear fit from da Cunha et al. 2010 is shown as a black dashed line). In Fig. 7, it can also be seen that the DDGs are among the most massive galaxies in our sample, and they host extremely small dust reservoirs, given their stellar masses, consistent with the assertion that DDGs represent genuine massive, elliptical galaxies, likely to host a hot, X-ray-emitting interstellar and/or intergalactic medium (Anderson et al. 2015).

Irregularities between stellar and gas kinematics favour a merger-driven explanation for the dust content of H-ATLAS-detected DDGs. In this scenario, these galaxies begin as typical quiescent ellipticals hosting very little molecular gas and dust (Leeuw et al. 2008; Young et al. 2011; Smith et al. 2012), thus occupying the upper left-hand side of Fig. 7. These galaxies will then undergo minor mergers with gas-rich satellites containing both star-forming gas and dust that is stripped by the central galaxy. A minor merger such as this will significantly increase $M_{\rm d}$ while contributing negligibly to M_*, thus moving galaxies horizontally towards the right-hand side. This is consistent with their location in Fig. 7, offset from HRS LTGs and RDGs. Observations have also shown that the star formation efficiency of gas stripped from galaxies can be extremely low (Knierman et al. 2013; Jáchym et al. 2014), consistent with $M_{\rm d}$ versus SFR for kinematic ETGs presented here.

RDGs more closely follow the relationship for normal star-forming galaxies of da Cunha et al. (2010) in Fig. 6 than DDGs, and have an $M_{\rm d}$–M_* relationship consistent with HRS LTGs. Although there are examples of suppressed star formation at a wide range of dust masses, these are found to be within the scatter of the SDSS data. Recently, Lianou et al. (2016) examined the scaling relations for ETGs in the HRS, finding a significantly larger scatter for ETGs than that observed by da Cunha et al. (2010), with galaxies typically deviating to low SFR, consistent with results presented here. A possible explanation for the position of low-SFR RDGs in Fig. 6 is morphological quenching (Martig et al. 2009), where the efficiency of converting molecular gas into stars is reduced in the presence of a massive bulge. This has been seen in observations previously (Saintonge et al. 2012) and, given the known correlation between M_* and B/T (e.g. Lang et al. 2014), can also explain why all three RDGs with $\log_{10}(M_*) > 10.8$ M$_\odot$ exhibit a low SFR with a retention of their dust content.

6 DISCUSSION

6.1 Moving beyond visual classification of galaxies

The dusty ETGs from A13/A15 studied here have been visually classified by both the GAMA team (Kelvin et al. 2014) and the SAMI team using essentially the same classification criteria. Two of the key differences between the classifications are that they are made up of independent groups of classifiers and they used different images in the classification process. GAMA classifications of Kelvin et al. (2014) are based on false colour g-, i- and H-band composite images, while SAMI classifications employ SDSS DR9 gri images. The use of longer wavelength data has resulted in the GAMA classifications tending somewhat towards earlier types. There is likely also an influence of the third key difference between SAMI and GAMA classifications, namely those of SAMI include signs of star formation (based on galaxy colour rather than morphology alone) to distinguish LTGs from ETGs. This would help to explain why such a large number of A13/A15 ETGs are identified as Sa galaxies, which are morphologically difficult to separate from S0 galaxies beyond $z = 0.05$, but would be identified by SAMI as later types due to their blue colours. This difference is illustrated in the top panel of Fig. 8, where we show the GAMA and SAMI classifications for the A13/A15 dusty ETGs studied here. We show classification histograms for H-ATLAS non-detections in the bottom panel of Fig. 8, and, although GAMA classifications are still slightly skewed towards earlier types, the level of agreement is improved compared to H-ATLAS detections.

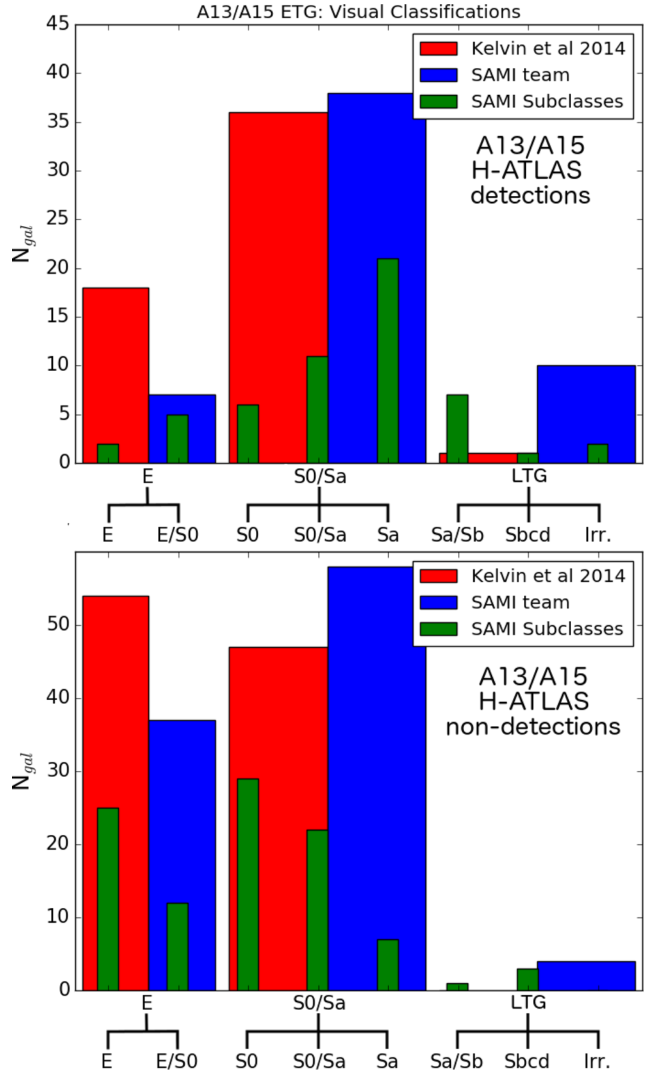

Figure 8. Comparison between visual morphologies from Kelvin et al. (2014) and those of the SAMI team. The classifications of Kelvin et al. (2014) are based on g-, i- and H-band images, while those of SAMI, using a similar classification scheme, are based on SDSS gri images from DR9. In both panels, large red and blue bars show broad classifications (E, S0/Sa and LTG) from the GAMA and SAMI teams, respectively, while small green bars show subclasses for the SAMI team. The upper axis labels correspond to the broad classes, while the lower labels correspond to SAMI subclasses. Top panel: classifications for H-ATLAS-detected ETGs from A13/A15. Bottom panel: classifications for H-ATLAS-non-detected galaxies as a control.

There is often an inherent assumption that there is a connection between the visual classification of a galaxy as an ETG and the presence of a hot, X-ray-emitting ISM (Rowlands et al. 2012; A13; Martini, Dicken & Storchi-Bergmann 2013; A15). This may not be fully justified, and, in the case of A13/A15, the inclusion of a large number of Sa galaxies makes this connection more dubious. Comparing those GAMA ETGs containing dust to those that do not, A13 show that dusty ETGs are bluer, less concentrated and have lower Sérsic indices. Further, A13 dusty ETGs have NUV$-r$ colours more similar to H-ATLAS-detected GAMA LTGs than to non-detected ETGs. Thus, from A13, there is already an indication that many H-ATLAS-detected visual ETGs from GAMA have properties more like LTGs than giant ellipticals hosting X-ray haloes.

The kinematic analysis of the 49 A13/A15 H-ATLAS detections with reliable SAMI observations agrees well with this assessment. In Section 5.1.1, we show that 44/49 of these galaxies have a V_c versus $\sigma_{\rm mean}$ in Fig. 4, suggesting kinematics largely dominated by rotation (termed RDGs here). All of these galaxies have $\sigma_{\rm mean}$ below 150 km s^{-1} (with only six above $\sigma_{\rm mean}$ = 100 km s^{-1}), the approximate value above which galaxies have X-ray luminosities exceeding the value expected for the cumulative emission from SN remnants and X-ray binaries in empirical studies (Boroson et al. 2011; Sarzi et al. 2013; Kim & Fabbiano 2015; Goulding et al. 2016).

It has also been shown by Anderson et al. (2015) that M_* can often be used to identify galaxies hosting an X-ray-emitting ISM, with the clearest evidence found for galaxies with $\log_{10}(M_*) > 10.8\ \mathrm{M}_{\odot}$. In fact, it is likely that M_* is more fundamental in determining the presence of such a hot ISM as it is the high mass concentration of these galaxies that prevents hot gas from escaping into the intergalactic medium. This means that $\sigma_{\rm mean}$ is a secondary indicator arising through the relationship between M_* and σ in ETGs (Faber & Jackson 1976). This connection occurs because massive ETGs derive their dynamical support from random motions, which is not the case for galaxies with significant rotation.

Assuming that M_* is a better indicator for the presence of hot X-ray-emitting gas than $\sigma_{\rm mean}$ in rotating galaxies, we also identify H-ATLAS-detected RDGs with $\log_{10}(M_*) > 10.8$ in Fig. 4. A total of 41/44 H-ATLAS -detected RDGs are found to have masses below this limit, supporting our assertion that they do not host a hot ISM. Although the remaining three RDGs are massive enough to host an X-ray-emitting halo, they are also found to have rapid rotation, with $V_c > 160$ km s^{-1} in all three cases. Negri et al. (2014a,b) have shown that rapid rotation allows massive galaxies to host a disc of cold gas even in the presence of an X-ray-emitting halo. This means that, regardless of the properties of the ISM in these three galaxies, dust residing in their discs can be long-lived; thus, an external origin for their dust content is unnecessary.

Thus, the visual classification of a galaxy as an ETG should not be assumed as clear evidence for the presence of a hot ISM, which is inhospitable to dust, in agreement with previous works (e.g. Sansom et al. 2000, 2006). In contrast, despite their appearance, many visually classified ETGs are actually rotationally supported, disc-like, star-forming galaxies with a relatively normal dust content comparable to galaxies found on the star-forming main sequence. In other words, the term early type in this case does not imply any structural difference, but mainly a difference in colour and possibly SFR. This means that the dust content of these galaxies is likely produced internally through normal processes such as SNe and stellar winds without the need for external mechanisms such as cooling flows or minor mergers.

6.2 DDGs, dust and merger rates

From our sample of 49 dusty ETGs from A13/A15 with reliable SAMI observations, we identify four galaxies in Fig. 4 that are kinematically consistent with being dispersion-dominated systems. SDSS DR9 images of these galaxies are shown in Fig. 5 alongside velocity and velocity dispersion maps from the SAMI Galaxy Survey. All four galaxies exhibit inconsistencies between their stellar and ionized gas, indicating recent stochastic processes such as gas accretion through merging. Galaxies 551505 and 534655 are found to have kinematic misalignments of $\sim 90^{\circ}$, while galaxies 508180 and 511892 have stellar-to-gas V_c ratios < 0.60, inconsistent with the range observed for asymmetric drift in LTGs (0.75–0.89; Martinsson et al. 2013; Cortese et al. 2016). Furthermore, the regular appearance of these galaxies from SDSS observations suggests that if mergers are responsible for these kinematic inconsistencies, then these mergers must either be minor, as major mergers typically result in disturbed morphologies (e.g. Larson et al. 2016), or they occurred in the fairly distant past, thus having allowed significant time for dynamical relaxation. A possible caveat, however, is that observations deeper than those from SDSS may reveal disturbed morphologies apparent as low-surface-brightness features (e.g. Sheen et al. 2012).

Evidence that the dust content of these four galaxies may have been recently accreted comes by comparing M_d to other galaxy properties. First, Fig. 6 shows that DDGs have suppressed SFR compared to normal star-forming galaxies, a feature seen in simulations of wet minor mergers (Peirani et al. 2010; Davis et al. 2015; Geréb et al. 2016). DDGs are also significantly offset above the M_d–M_* relationship for star-forming galaxies shown in Fig. 7, similar to dusty ETGs from Dariush et al. (2016), who observe little variation in M_* with varying M_d. This lack of a correlation is suggested as further evidence of external accretion. Indeed, extremely dust-poor massive elliptical galaxies will fall far above the M_d–M_* trend for star-forming galaxies, occupying the top left-hand region of Fig. 7. A subsequent wet minor merger will provide a negligible increase in M_* while significantly increasing M_d; thus, the merger remnants will move horizontally to the right-hand region in Fig. 7 towards the region occupied by kinematic ETGs discussed here.

Assuming that all four H-ATLAS-detected DDGs in this work have acquired their dust content in a merger, how do our results compare with expectations based on the cosmological rates of mergers at low redshift? Martini et al. (2013) compare the measured rate of minor mergers to the theoretical estimates of the destruction time for dust in hot gas of Draine & Salpeter (1979). Following Stewart et al. (2009), the authors make a rough prediction of the expected fraction of dusty ETGs, $f_{\rm dust}$, based on estimates of the merger rate of $R_{\rm merg}$ = 0.07–0.2 Gyr^{-1} and a dust lifetime of $\tau_{\rm dust} < 0.02$ Gyr following

$$f_{\rm dust} = R_{\rm merg}\tau_{\rm dust}. \tag{3}$$

This gives $f_{\rm dust} < 0.14$–0.4 per cent, implying that a purely external accretion scenario for large samples of dusty ETGs is extremely unlikely from a statistical perspective. The results of our study provide a possible solution to this tension. First, we note that the fraction of ETGs with dust quoted by Martini et al. (2013) is 0.6, whereas for GAMA ETGs in A13, there is only a 29 per cent detection rate from the H-ATLAS survey. As we have shown, however, many of these galaxies are kinematically inconsistent with the presence of a hot ISM. Among DDGs, we find an even lower H-ATLAS detection rate of 11 per cent (4/35), a factor of $\sim$5 lower than the value assumed by Martini et al. (2013), yet still significantly larger than their predicted value of $f_{\rm dust} < 0.14$ per cent.

The argument of Martini et al. (2013), however, is dependent on a number of assumptions regarding the time-scales and conditions of dust accretion in ETGs. Some works have estimated a time-scale for gas stripping of the order of a few times 10^8 yr (Takeda, Nulsen & Fabian 1984; Murakami & Babul 1999), which could further increase $f_{\rm dust}$ predictions by an order of magnitude to $\sim$1.4–4.0 per cent. The remaining tension between this estimate and the estimate of $f_{\rm dust}$ = 11 per cent found in this work may be partially due to incompleteness as a result of our small sample size. Another possibility though is the recent suggestion that accretion of dust that is embedded in a larger cold medium may be shielded from the harsh ISM, resulting in a further significant increase in dust lifetimes (e.g. Clemens et al. 2010; Dasyra et al. 2012; Finkelman et al. 2012).

A full understanding of just how much longer dust may survive in such a scenario is beyond the scope of this work. It should also be noted that, in those galaxies with $V_{c,star}/V_{c,gas} < 0.6$, the fact that the gas is kinematically aligned with the stars suggests that if the presence of the dust is truly the result of a merger, then it must have had sufficient time to undergo dynamic relaxation. This process should occur on Gyr time-scales (Lake & Norman 1983; Davis & Bureau 2016), supporting the idea that the direct, sub-galactic, environment of dust in ETGs may drastically increase the lifetime of interstellar dust.

We can also discuss the comparison between stellar and ionized gas kinematics of dust-free DDGs in this study, i.e. H-ATLAS non-detections from A13/A15. Of the 31 H-ATLAS-non-detected DDGs included here, 36 per cent (11/31) show signs of kinematic discrepancies between their ionized gas and stars. Among these 11, 7/11 are kinematically misaligned, while 4/11 are aligned with significantly larger gas V_c compared to that of the stars. The remaining 20 galaxies, however, do not have secure enough detections of ionized gas to provide clean ionized gas kinematics maps. Considering our entire sample of 540 SAMI galaxies with high-quality stellar kinematics observations, we find a total subsample of 71 DDGs. Out of these, 49 per cent (35/71) show kinematic irregularities; however, only 58 per cent (41/71) have strong ionized gas detections. Among the 35 kinematically irregular DDGs, 22 are kinematically misaligned, while the remaining 13 have aligned ionized gas rotating significantly faster than the stars. Our finding that 54 per cent (22/41) of DDGs with appreciable amounts of ionized gas are kinematically misaligned agrees well with the findings of Bryant et al. (in preparation), who find that, among a larger sample of SAMI galaxies, 40–53 per cent of ETGs with high-S/N ionized gas emission exhibit kinematically misaligned gas.

This begs the question: How are kinematically irregular, H-ATLAS-non-detected DDGs related to DDGs with H-ATLAS detections? The strongest statement we can make in this regard is that the presence of dust does not have a large impact on the relative dynamics of gas and stars in DDGs with significant gas. As we do not have strong constraints on the possible dust content of H-ATLAS-non-detected galaxies, unlike H-ATLAS detections, we do not have the secondary indications of mergers as an explanation for their kinematic irregularity (e.g. M_d versus M_*). We can simply say that the presence of ionized gas is likely associated with a stochastic process that has also affected the gas kinematics in these galaxies. Unlike dust, however, ionized gas is not always directly associated with cold gas in galaxies. Indeed, a number of works have shown that old stellar populations (such as post-AGB stars), active galactic nuclei, or even interactions between warm and hot (X-ray-emitting) gas phases may be the dominant sources of ionized gas emission in ETGs (e.g. Binette et al. 1994; Sarzi et al. 2010; Yan & Blanton 2012). This means that the detection of ionized gas emission in the absence of a secure detection of cold dust is not inconsistent with the presence of a hot, X-ray-emitting ISM.

A caveat here, however, is that some H-ATLAS-non-detected galaxies from A13/A15 (particularly those DDGs with strong ionized gas emission) may contain appreciable amounts of dust, but have far-IR fluxes below the sensitivity limits of H-ATLAS. Assuming that the presence of ionized gas is *always* associated with dust in our sample of SAMI galaxies would increase our estimate of the number of DDGs with dust to 58 per cent (41/71). Thus, the level of tension between merger rates and dust lifetimes in ETGs here would roughly match that seen by Martini et al. (2013). This assumption, however, is unfounded, and, as we have noted, estimates of dust lifetimes in the presence of a complex, multiphase ISM in ETGs are equally uncertain. Further study of the ISM of massive galaxies and the precise conditions of gas accretion on to these systems will be required to understand the underlying cause of this tension.

Finally, we note that out of the 41 DDGs from our full SAMI sample that exhibit appreciable ionized gas emission, 5 do not show clear discrepancies between ionized gas and stellar kinematics. These galaxies, however, have not been observed by H-ATLAS; thus, the presence of dust is uncertain. Given the above discussion regarding sources of ionizing radiation in ETGs, unless these galaxies can be shown to host cold gas or dust, they should not be considered to be peculiar objects.

7 SUMMARY

In this paper, we have analysed the 2D kinematics of visually classified ETGs from A13 and A15 using IFS data from the SAMI Galaxy Survey. The sample of A13/A15 includes 220 H-ATLAS detected (dusty) galaxies and 551 H-ATLAS-non-detected (dust-free) galaxies. We begin by measuring the stellar circular velocity, V_c, and flux-weighted, global, stellar velocity dispersion, σ_{mean}, for a sample of 540 SAMI galaxies for which we can measure V_c beyond the turnover radius of the rotation curve. These values provide a kinematic selection designed to determine those visual ETGs that are consistent with having dispersion-dominated stellar kinematics, indicative of the presence of a hot, X-ray-emitting ISM. This selection is then applied to visually classified ETGs from A13/A15 that have currently been observed with SAMI. Finally, we examine the dust properties of these galaxies in comparison with our kinematic selection in order to better understand the origin of the dust in these systems. Our key results are as follows:

(i) Selecting A13/A15 ETGs based on V_c and σ_{mean}, we find that 11 per cent (4/35) of dispersion-dominated A13/A15 galaxies are H-ATLAS detected. This is in contrast to the 29 per cent (220/771) detection rate for the full A13/A15 sample and 40 per cent (45/113) for RDGs. Thus, the detection of dust in visually classified ETGs is 3.5 times more likely in galaxies with disc-like rotation than in those with kinematics more consistent with massive elliptical galaxies.

(ii) Similarly, only 8 per cent (4/49) of H-ATLAS-detected ETGs from A13/A15 with SAMI observations are kinematically consistent with being trueDDGs. The remainder have kinematics more similar to blue, visually classified LTGs and S0/Sa galaxies.

(iii) 100 per cent of these dispersion-dominated, dusty ETGs exhibit inconsistencies between their stellar and ionized gas kinematics, suggestive of recent merger activity and an external origin for their dust content. The corresponding rate of gas versus stellar kinematic discrepancies in our full sample of dispersion-dominated SAMI galaxies is 45 per cent (34/75).

(iv) The four dispersion-dominated, dusty ETGs in our sample are also extremely massive and thus quite likely to host a hot, X-ray-emitting halo. As such, an external accretion scenario is the most viable source for their dust content. Observations of a suppressed star formation in these four galaxies, typical of gas accreted on to massive galaxies (e.g. Geréb et al. 2016), further supports this assertion.

(v) The low velocity dispersions as well as low masses and/or rapid rotation of the remaining galaxies suggest that dust in these systems may be long-lived, thereby eliminating any need for an external scenario for the origin of their dust content.

We have shown that these results may help to reduce the tension between expected dust lifetimes in massive ETGs (Draine & Salpeter 1979; Clemens et al. 2010), observed merger rates

(Lotz et al. 2011) and the observed number of visual ETGs containing dust (Martini et al. 2013). A more complete understanding of the complex, multiphase ISM of massive ETGs, as well as the exact conditions through which gas is accreted on to these systems, will be necessary in understanding this tension fully.

ACKNOWLEDGEMENTS

RB acknowledges support under the Australian Research Council's (ARC) Discovery Projects funding scheme (DP130100664). JvdS is funded under Bland-Hawthorn's ARC Laureate Fellowship (FL140100278). SMC acknowledges the support of an Australian Research Council Future Fellowship (FT100100457). SB acknowledges the funding support from the Australian Research Council through a Future Fellowship (FT140101166). Support for AMM is provided by NASA through a Hubble Fellowship grant #HST-HF2-51377 awarded by the Space Telescope Science Institute, which is operated by the Association of Universities for Research in Astronomy, Inc., for NASA, under contract NAS5-26555. MSO acknowledges the funding support from the Australian Research Council through a Future Fellowship Fellowship (FT140100255). We would also like to thank the anonymous referee for comments and suggestions that have improved the clarity and readability of this work. The SAMI Galaxy Survey is based on observations made at the Anglo-Australian Telescope. SAMI was developed jointly by the University of Sydney and the Australian Astronomical Observatory. The SAMI input catalogue is based on data taken from the SDSS, the GAMA Survey and the VST ATLAS Survey. The SAMI Galaxy Survey is funded by the Australian Research Council Centre of Excellence for All-sky Astrophysics (CAASTRO), through project number CE110001020, and other participating institutions. The SAMI Galaxy Survey website is http://sami-survey.org/. GAMA is a joint European–Australasian project based around a spectroscopic campaign using the Anglo-Australian Telescope. The GAMA input catalogue is based on data taken from the SDSS and the UKIRT Infrared Deep Sky Survey. Complementary imaging of the GAMA regions is being obtained by a number of independent survey programmes, including *GALEX* MIS, VST KiDS, VISTA VIKING, *WISE*, H-ATLAS, GMRT and ASKAP providing UV to radio coverage. GAMA is funded by the STFC (UK), the ARC (Australia), the AAO and the participating institutions. The GAMA website is http://www.gama-survey.org/.

REFERENCES

Agius N. K. et al., 2013, MNRAS, 431, 1929 (A13)
Agius N. K. et al., 2015, MNRAS, 451, 3815 (A15)
Anderson M. E., Gaspari M., White S. D. M., Wang W., Dai X., 2015, MNRAS, 449, 3806
Athey A., Bregman J., Bregman J., Temi P., Sauvage M., 2002, ApJ, 571, 272
Balcells M., Quinn P. J., 1990, ApJ, 361, 381
Baldry I. K. et al., 2010, MNRAS, 404, 86
Bassett R., Bekki K., Cortese L., Couch W. J., 2017, preprint (arXiv:e-prints)
Bassett R. et al., 2014, MNRAS, 442, 3206
Bekki K., 1998, ApJ, 499, 635
Bekki K., Shioya Y., 2000, A&A, 362, 97
Bendo G. J., Barnes J. E., 2000, MNRAS, 316, 315
Binette L., Magris C. G., Stasińska G., Bruzual A. G., 1994, A&A, 292, 13
Bland-Hawthorn J. et al., 2011, Opt. Exp., 19, 2649
Boroson B., Kim D.-W., Fabbiano G., 2011, ApJ, 729, 12
Boselli A. et al., 2010, PASP, 122, 261
Bregman J. N., Miller E. D., Athey A. E., Irwin J. A., 2005, ApJ, 635, 1031
Bruzual G., Charlot S., 2003, MNRAS, 344, 1000
Bryant J. J., Bland-Hawthorn J., Fogarty L. M. R., Lawrence J. S., Croom S. M., 2014, MNRAS, 438, 869
Bryant J. J. et al., 2015, MNRAS, 447, 2857
Cappellari M., 2016, ARA&A, 54, 597
Cappellari M., Emsellem E., 2004, PASP, 116, 138
Cappellari M. et al., 2011, MNRAS, 413, 813
Clemens M. S. et al., 2010, A&A, 518, L50
Cortese L. et al., 2012, A&A, 540, A52
Cortese L. et al., 2014, ApJ, 795, L37
Cortese L. et al., 2016, MNRAS, 463, 170
Croom S. M. et al., 2012, MNRAS, 421, 872
da Cunha E., Charlot S., Elbaz D., 2008, MNRAS, 388, 1595
da Cunha E., Eminian C., Charlot S., Blaizot J., 2010, MNRAS, 403, 1894
Dariush A. et al., 2016, MNRAS, 456, 2221
Dasyra K. M., Combes F., Salomé P., Braine J., 2012, A&A, 540, A112
Davies L. J. M. et al., 2016, MNRAS, 455, 4013
Davis T. A., Bureau M., 2016, MNRAS, 457, 272
Davis T. A. et al., 2011, MNRAS, 417, 882
Davis T. A. et al., 2014, MNRAS, 444, 3427
Davis T. A. et al., 2015, MNRAS, 449, 3503
de Blok W. J. G., Walter F., Brinks E., Trachternach C., Oh S.-H., Kennicutt R. C., Jr, 2008, AJ, 136, 2648
Di Matteo P., Combes F., Melchior A.-L., Semelin B., 2007, A&A, 468, 61
di Serego Alighieri S. et al., 2013, A&A, 552, A8
Draine B. T., Salpeter E. E., 1979, ApJ, 231, 77
Driver S. P. et al., 2009, Astron. Geophys., 50, 12
Driver S. P. et al., 2011, MNRAS, 413, 971
Driver S. P. et al., 2016, MNRAS, 455, 3911
Driver S. P. et al., 2017, GAMA/G10-COSMOS/3D-HST: The Cosmic Star-Formation History, and the Build Up of Stars and Dust, preprint (arXiv:e-prints)
Dunne L. et al., 2011, MNRAS, 417, 1510
Dye S. et al., 2010, A&A, 518, L10
Eales S. et al., 2010, PASP, 122, 499
Emsellem E. et al., 2007, MNRAS, 379, 401
Emsellem E. et al., 2011, MNRAS, 414, 888
Epinat B. et al., 2009, A&A, 504, 789
Fabbiano G., 2006, ARA&A, 44, 323
Faber S. M., Jackson R. E., 1976, ApJ, 204, 668
Fabian A. C., Crawford C. S., Edge A. C., Mushotzky R. F., 1994, MNRAS, 267, 779
Finkelman I., Brosch N., Funes J. G., Barway S., Kniazev A., Väisänen P., 2012, MNRAS, 422, 1384
Fogarty L. M. R. et al., 2015, MNRAS, 454, 2050
Geréb K., Catinella B., Cortese L., Bekki K., Moran S. M., Schiminovich D., 2016, MNRAS, 462, 382
Gomez A., Mennessier M. O., 1977, A&A, 54, 113
Gomez H. L. et al., 2010, A&A, 518, L45
Goudfrooij P., Trinchieri G., 1998, A&A, 330, 123
Goulding A. D. et al., 2016, ApJ, 826, 167
Graham A. W., Worley C. C., 2008, MNRAS, 388, 1708
Green A. W. et al., 2014, MNRAS, 437, 1070
Haan S. et al., 2013, MNRAS, 434, 1264
Hildebrand R. H., 1983, Q. J. R. Astron. Soc., 24, 267
Ho I.-T. et al., 2014, MNRAS, 444, 3894
Ho I.-T. et al., 2016a, Ap&SS, 361, 280
Ho I.-T. et al., 2016b, MNRAS, 457, 1257
Hopkins P. F., Hernquist L., Cox T. J., Di Matteo T., Robertson B., Springel V., 2006, ApJS, 163, 1
Iodice E., Capaccioli M., Spavone M., Napolitano N. R., Grado A., Limatola L., Cantiello M., Schipani P., 2015, A&A, 574, A111
Itoh H., 1989, PASJ, 41, 853
Jáchym P., Combes F., Cortese L., Sun M., Kenney J. D. P., 2014, ApJ, 792, 11
Jimmy Tran K.-V., Brough S., Gebhardt K., von der Linden A., Couch W. J., Sharp R., 2013, ApJ, 778, 171
Jones T. A., Swinbank A. M., Ellis R. S., Richard J., Stark D. P., 2010,

MNRAS, 404, 1247
Kauffmann G. et al., 2003, MNRAS, 341, 33
Kaviraj S., Peirani S., Khochfar S., Silk J., Kay S., 2009, MNRAS, 394, 1713
Kaviraj S. et al., 2013, MNRAS, 435, 1463
Kelvin L. S. et al., 2014, MNRAS, 444, 1647
Kim D.-W., Fabbiano G., 2015, ApJ, 812, 127
Knapp G. R., 1985, ApJ, 293, 273
Knapp G. R., Guhathakurta P., Kim D.-W., Jura M. A., 1989, ApJS, 70, 329
Knapp G. R., Gunn J. E., Wynn-Williams C. G., 1992, ApJ, 399, 76
Knierman K. A., Scowen P., Veach T., Groppi C., Mullan B., Konstantopoulos I., Knezek P. M., Charlton J., 2013, ApJ, 774, 125
Krajnović D., Cappellari M., de Zeeuw P. T., Copin Y., 2006, MNRAS, 366, 787
Lagos C. D. P., Davis T. A., Lacey C. G., Zwaan M. A., Baugh C. M., Gonzalez-Perez V., Padilla N. D., 2014, MNRAS, 443, 1002
Lake G., Norman C., 1983, ApJ, 270, 51
Lambas D. G., Maddox S. J., Loveday J., 1992, MNRAS, 258, 404
Lang P. et al., 2014, ApJ, 788, 11
Larson K. L. et al., 2016, ApJ, 825, 128
Law D. R., Steidel C. C., Erb D. K., Larkin J. E., Pettini M., Shapley A. E., Wright S. A., 2009, ApJ, 697, 2057
Leeuw L. L., Davidson J., Dowell C. D., Matthews H. E., 2008, ApJ, 677, 249
Lemoine-Busserolle M., Lamareille F., 2010, MNRAS, 402, 2291
Lianou S., Xilouris E., Madden S. C., Barmby P., 2016, MNRAS, 461, 2856
Liske J. et al., 2015, MNRAS, 452, 2087
Lotz J. M., Jonsson P., Cox T. J., Croton D., Primack J. R., Somerville R. S., Stewart K., 2011, ApJ, 742, 103
McDermid R. M. et al., 2006, MNRAS, 373, 906
Ma C.-P., Greene J. E., McConnell N., Janish R., Blakeslee J. P., Thomas J., Murphy J. D., 2014, ApJ, 795, 158
Martig M., Bournaud F., Teyssier R., Dekel A., 2009, ApJ, 707, 250
Martini P., Dicken D., Storchi-Bergmann T., 2013, ApJ, 766, 121
Martinsson T. P. K., Verheijen M. A. W., Westfall K. B., Bershady M. A., Schechtman-Rook A., Andersen D. R., Swaters R. A., 2013, A&A, 557, A130
Mathews W. G., Brighenti F., 2003, ApJ, 590, L5
Matsuura M. et al., 2009, MNRAS, 396, 918
Mineo S., Gilfanov M., Sunyaev R., 2012, MNRAS, 419, 2095
Mulchaey J. S., Jeltema T. E., 2010, ApJ, 715, L1
Murakami I., Babul A., 1999, MNRAS, 309, 161
Nanni A., Bressan A., Marigo P., Girardi L., 2013, MNRAS, 434, 2390
Negri A., Ciotti L., Pellegrini S., 2014a, MNRAS, 439, 823
Negri A., Posacki S., Pellegrini S., Ciotti L., 2014b, MNRAS, 445, 1351
Newman S. F. et al., 2012, ApJ, 761, 43
Noordermeer E., 2006, PhD thesis, Rijksuniversiteit
Ortiz-Gil A., Guzzo L., Schuecker P., Böhringer H., Collins C. A., 2004, MNRAS, 348, 325
Padilla N. D., Strauss M. A., 2008, MNRAS, 388, 1321
Peirani S., Crockett R. M., Geen S., Khochfar S., Kaviraj S., Silk J., 2010, MNRAS, 405, 2327
Pracy M. B., Couch W. J., Blake C., Bekki K., Harrison C., Colless M., Kuntschner H., de Propris R., 2005, MNRAS, 359, 1421
Rampazzo R., Annibali F., Bressan A., Longhetti M., Padoan F., Zeilinger W. W., 2005, A&A, 433, 497
Rigby E. E. et al., 2011, MNRAS, 415, 2336
Rowlands K. et al., 2012, MNRAS, 419, 2545
Saintonge A. et al., 2012, ApJ, 758, 73
Sanders D. B., Surace J. A., Ishida C. M., 1999, in Barnes J. E., Sanders D. B., eds, Proc. IAU Symp. 186, Galaxy Interactions at Low and High Redshift. Kluwer, Dordrecht, p. 289
Sansom A. E., Hibbard J. E., Schweizer F., 2000, AJ, 120, 1946
Sansom A. E., O'Sullivan E., Forbes D. A., Proctor R. N., Davis D. S., 2006, MNRAS, 370, 1541
Sarzi M. et al., 2010, MNRAS, 402, 2187
Sarzi M. et al., 2013, MNRAS, 432, 1845
Shabala S. S. et al., 2012, MNRAS, 423, 59
Sharp R. et al., 2006, in McLean I. S., Iye M., eds, Proc.SPIE Conf. Ser. Vol. 6269, Ground-Based and Airborne Instrumentation for Astronomy. SPIE, Bellingham, p. 62690G
Sheen Y.-K., Yi S. K., Ree C. H., Lee J., 2012, ApJS, 202, 8
Simard L. et al., 2002, ApJS, 142, 1
Simard L., Mendel J. T., Patton D. R., Ellison S. L., McConnachie A. W., 2011, ApJS, 196, 11
Smith M. W. L. et al., 2012, ApJ, 748, 123
Stewart K. R., Bullock J. S., Wechsler R. H., Maller A. H., 2009, ApJ, 702, 307
Su Y., Irwin J. A., White R. E., III, Cooper M. C., 2015, ApJ, 806, 156
Takeda H., Nulsen P. E. J., Fabian A. C., 1984, MNRAS, 208, 261
Temi P., Brighenti F., Mathews W. G., 2007, ApJ, 660, 1215
Thakar A. R., Ryden B. S., Jore K. P., Broeils A. H., 1997, ApJ, 479, 702
Tsai J. C., Mathews W. G., 1995, ApJ, 448, 84
van de Sande J. et al., 2017, ApJ, 835, 104
van de Voort F., Davis T. A., Kereš D., Quataert E., Faucher-Giguère C.-A., Hopkins P. F., 2015, MNRAS, 451, 3269
Weijmans A.-M. et al., 2014, MNRAS, 444, 3340
Weiner B. J. et al., 2006, ApJ, 653, 1027
Westfall K. B., Bershady M. A., Verheijen M. A. W., Andersen D. R., Swaters R. A., 2007, Astrophys. Space Sci. Proc., 3, 157
Williams M. J., Bureau M., Cappellari M., 2010, MNRAS, 409, 1330
Wisnioski E. et al., 2011, MNRAS, 417, 2601
Wu X.-P., Xue Y.-J., Fang L.-Z., 1999, ApJ, 524, 22
Yan R., Blanton M. R., 2012, ApJ, 747, 61
York D. G. et al., 2000, AJ, 120, 1579
Young L. M. et al., 2011, MNRAS, 414, 940
Zhang Y.-Y., Andernach H., Caretta C. A., Reiprich T. H., Böhringer H., Puchwein E., Sijacki D., Girardi M., 2011, A&A, 526, A105

APPENDIX A: DUST MASS UPPER LIMITS FOR H-ATLAS NON-DETECTIONS

As described in Section 3.2, $M_{\rm d}$ for H-ATLAS-detected galaxies is measured by the GAMA survey team using the MAGPHYS spectral fitting code of da Cunha et al. (2008). MAGPHYS relies on detections in the far-IR in order to provide reliable estimates of $M_{\rm d}$; therefore, those $M_{\rm d}$ values provided by MAGPHYS for H-ATLAS-non-detected galaxies are highly uncertain. Thus, for these galaxies, we estimate upper limits on the dust masses in the following manner:

First, we take the upper limit for the flux in the 250 μm *Herschel* SPIRE band, F_{250}, to be ∼33 mJy (Dunne et al. 2011). This is then converted to an upper limit on $M_{\rm d}$ using (Hildebrand 1983)

$$M_{\rm d} = \frac{F_{250} D_{\rm L}^2 K_{250}}{\kappa_{250} B(1+z)(T_{\rm d})_{250}}, \tag{A1}$$

where $D_{\rm L}$ is the luminosity distance to each galaxy, computed from spectroscopic redshifts, κ_{250} is the mass absorption coefficient assumed to be 0.89 m^2 kg^{-1} at 250 μm (Dunne et al. 2011), and $B(T_{\rm d})_{250}$ is the Planck function at 250 μm and at dust temperature $T_{\rm d}$. For all non-detected galaxies, we simply fix $T_{\rm d}$ at 22.1 K, the average value computed through grey-body fitting for H-ATLAS-detected sources from A13. Equation (A1) also includes a factor of (1+z) and a K-correction, which is given by

$$K = \left(\frac{\nu_{\rm obs}}{\nu_{\rm rf}}\right)^{3+\beta} \frac{{\rm e}^{(h\nu_{\rm rf}/kT_{\rm d})}-1}{{\rm e}^{h\nu_{\rm obs}/kT_{\rm d}}-1}, \tag{A2}$$

where $\nu_{\rm obs}$ and $\nu_{\rm rf}$ are the observed and rest-frame frequency, β is the dust emissivity index (fixed at 1.5; Dye et al. 2010), h is the Planck constant and k is the Boltzmann constant. $M_{\rm d}$ upper limits are depicted alongside MAGPHYS dust masses for H-ATLAS detections in Section 5.2.

APPENDIX B: ROTATION CURVE EXTRACTION AND MEASUREMENT OF V_C

After measuring the kinematic PA of our kinematics maps, we use this value as input in extracting the rotation curves for each galaxy. This is done by first determining the x and y positions of the galaxy centre from the stellar flux maps, $F(x, y)$ using

$$x_c = \frac{\sum_i \sum_j i \times F(i,j)}{\sum_i \sum_j F(i,j)} \quad ; \quad y_c = \frac{\sum_i \sum_j j \times F(i,j)}{\sum_i \sum_j F(i,j)}, \qquad \text{(B1)}$$

where x_c and y_c are the x and y positions of the galaxy centre. An artificial slit with a width of 1.5 arcsec (3 spaxels) is traced across the stellar velocity map with its position defined by the measured PA and galaxy centre. Examples of these artificial slits are shown in green in the right-hand column of Fig. B1. The radius $r(x, y)$ and velocity $v(x, y)$ are recorded at each spaxel within the slit. Here we define $r(x,y) = \sqrt{(x-x_c)^2 + (y-y_c)^2}$ with the sign taken to match the sign of $x - x_c$. The choice of the definition of positive and negative radii is arbitrary, however, as this simply defines a positive or negative V_c. In the end, the final value of the circular velocity is taken as $|V_c|$.

The stellar rotation curves extracted in this way are then used to determine the rotation velocity following the procedure of Epinat et al. (2009). This is done by fitting a piecewise function of the form

$$V(r) = \begin{cases} -V_c, & r \le -r_t \\ V_c(r/r_t), & -r_t < r < r_t, \\ V_c & r_t \le r \end{cases} \qquad \text{(B2)}$$

where r_t is the turnover radius of the rotation curve that defines where the flat portion of the rotation curve begins. This value is left as a free parameter. Examples of these fits for galaxies with low and high (apparent) V_c are shown in the left-hand column of Fig. B1. Although a fairly common feature of galaxy rotation curves is a decline in V_c beyond the turnover radius, r_t (e.g. de Blok et al. 2008), the coverage of our data cubes often does not extend to large enough radii to capture this behaviour. Thus, we choose to use the relatively simple model given in equation (B2) as including more parameters is more likely to result in spurious fits, particularly for low-S/N spaxels at large radii.

This procedure has the inherent assumption that the ~8.0 arcsec covered by SAMI data cubes is larger than r_t, which is not true for many galaxies. We check whether or not observations of each galaxy extend beyond r_t to test this. For each galaxy, we first identify the spaxel in our traced slit that is farthest from (x_c, y_c). If the radius measured for this spaxel is larger than r_t, then we flag this as a reliable measurement of V_c. We also visually inspect the rotation curve fits for each galaxy flagged as reliable for verification, and in this process, a small number of galaxies were identified with spurious fits and subsequently flagged and removed from our sample. Finally, some SAMI observations include a low number of spaxels with high-S/N data, which will reduce the reliability of our fitted value of V_c. We perform a test using galaxies with high-fidelity rotation curves in which we incrementally reduce the artificial slit length by 1 spaxel and remeasure V_c. We find that for slits containing more than 30 spaxels, we are able to recover V_c measured from the full slit for >95 per cent of galaxies tested. This fraction falls off rapidly below 30 spaxels; thus, galaxies for which slits contain less than 30 spaxels are excluded from our analysis. Among the 753 galaxies tested, we find that 554 galaxies meet these requirements.

We next correct our stellar V_c measurements for the effects of inclination, which causes observed V_cs to be lower than the intrinsic rotation velocity of a given galaxy. First, we determine the inclination of each galaxy using

$$\cos^2 i = \frac{(1-\epsilon)^2 - \alpha^2}{1 - \alpha^2}, \qquad \text{(B3)}$$

where i is the galaxy inclination, ϵ is the observed ellipticity and α is the intrinsic flattening for a given galaxy. For each galaxy, we provide a rough estimate of α based on the following criteria: First, we separate galaxies into those that are strongly disc-dominated from those with a significant influence from a central bulge. The former are identified as having B/T less than 0.3, while the latter have B/T larger than 0.3, which roughly follows the findings of Graham & Worley (2008). Here we take B/T from r-band values of Simard et al. (2011), who perform 2D bulge+disc decompositions for SDSS galaxies using the GIM2D software (v3.2; Simard et al. 2002). For disc-dominated galaxies, we fix α at 0.23, which is the average value found when comparing α values reported for spiral galaxies by Lambas, Maddox & Loveday (1992) and Padilla & Strauss (2008). Galaxies with B/T > 0.3 are then separated into pure ellipticals and S0/Sa galaxies based on SAMI morphological classifications. We assign an α of 0.55 to the S0 and Sa classes (Lambas et al. 1992; Noordermeer 2006) and a value of 0.63 to elliptical galaxies, the former being the average value found for slow rotators in the ATLAS^{3D} survey (Weijmans et al. 2014). This large α value for elliptical galaxies is appropriate because these objects appear relatively round even when the viewing angle is perpendicular to the axis of rotation. Galaxies with low intrinsic rotation and a spheroidal shape, for example, would have V_c significantly overestimated if it is assumed that the galaxy is much flatter. Thus, adopting $\alpha = 0.63$ for elliptical galaxies provides a conservative V_c correction appropriate for dispersion-supported galaxies. The exact assumptions regarding α will have only a minor effect on our results

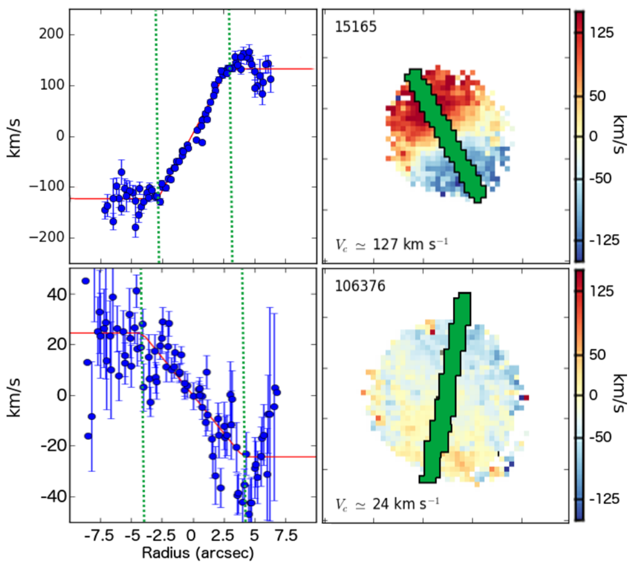

Figure B1. Two examples of our fitting procedure for V_c. The right-hand column illustrates, in green, the artificial slits that are traced along the kinematic major axis of our stellar velocity maps (box size = 25.0 arcsec) and the left-hand column shows as blue circles the individual velocities of pixels within the slit. Also shown in the left-hand column as solid red lines are rotation curve models for each galaxy given by equation (B1), and the green dotted lines indicate the locations of the turnover radii, r_t. We have chosen these two examples to show a rapidly rotating galaxy with a well-defined rotation curve (top row) as well as a much more slowly rotating galaxy (bottom row) roughly at the two extremes of our V_c measurements.

as this value is used to correct V_c, while, as we will show in Section 4.3, our kinematic selection is primarily based on stellar velocity dispersion.

Finally, we compute the inclination corrected stellar V_c, $V_{c,corr}$, as

$$V_{c,corr} = \frac{V_c}{(1+z)\sin i}. \tag{B4}$$

This correction inherently assumes that galaxies observed face-on are perfectly circular, which is certainly not accurate for all galaxies. By construction, this process has a relatively small effect on ETGs, while LTGs may have V_c underestimated by up to 270 km s^{-1}. This is typically the case galaxies observed close to face-on, for which V_c is already quite uncertain, however. Among the 563 galaxies with well-sampled rotation curves, we find a median increase in V_c due to our inclination correction of 4.7 km s^{-1}, and only 7 per cent have an increase in V_c of more than 50 km s^{-1}. As we are interested in ETGs in this work, cases like this will not affect our results.

APPENDIX C: σ_{mean}: MASKING AND BEAM-SMEARING CORRECTION

In this appendix, we describe in detail our methods of masking bad spaxels prior to measuring σ_{mean} and correcting σ_{mean} for the effects of seeing, commonly referred to as beam smearing.

We define bad spaxels as those that do not satisfy $\sigma_{error} < \sigma \times 0.1 + 25$ km s^{-1}. This requires the measured error in σ in each spaxel to be smaller than a fraction of the measured σ. The inclusion of the +25 km s^{-1} is needed so that we do not exclude a majority of spaxels with a low measurement of σ. Finally, we also exclude spaxels with $\sigma < 35$ km s^{-1}, which is the limit to which we trust our measurements (see van de Sande et al. 2017, for more details and for more on tests of our PPXF procedure). σ_{mean} is then measured as the flux-weighted velocity dispersion over unmasked spaxels in our stellar velocity dispersion maps. Formally, this is defined as follows:

Our measurements of σ_{mean} employ all spaxels meeting the quality cut described above. We test the robustness of σ_{mean} by remeasuring this value within radii between 1.0 and 8.0 arcsec (2–16 spaxels). We find that σ_{mean} measurements level off beyond 1.5 arcsec, and remain unchanged out to 8.0 arcsec. This means that σ_{mean} measurements are robust for all galaxies that meet our V_c quality cut, i.e. velocities are measured beyond r_t.

The major difficulty in estimating the global velocity dispersions from IFS observations is accounting for the effects of beam smearing, which can artificially inflate σ measured in individual spaxels (e.g. Pracy et al. 2005; Law et al. 2009). This effect is enhanced in the central regions of rapidly rotating galaxies where large velocity gradients are observed over individual spaxels. Beam smearing is a complex effect, acting in all three dimensions of IFS data cubes, and a significant ongoing effort to understand beam smearing in SAMI data is underway. In the meantime, we perform a simple beam-smearing correction on σ_{mean} following Bassett et al. (2014). For each galaxy, we estimate the additional σ induced by beam smearing, σ_{bs}, as

$$\sigma_{bs} \approx \frac{dV}{d\theta}\sigma_\theta, \tag{C1}$$

where dV is the velocity gradient defined by our V_c fits as V_c/r_t (see Section 4.1), dθ is the spaxel size of 0.5 arcsec and σ_θ is the seeing of our observations. Seeing values for SAMI galaxies are catalogued at the time of observation with the median seeing at the AAT site being 1.8 arcsec. We estimate a 'beam-smearing-corrected' σ_{mean} as $\sigma_{m,corr} = \sqrt{\sigma^2_{mean} - \sigma^2_{bs}}$. The typical corrections measured in this way reduce the measured σ_{mean} by ∼0–30 km s^{-1} with a clear dependence on V_c. Below $V_c = 60$ km s^{-1}, corrections are closer to ∼0–5 km s^{-1}. Note that this may result in measured values of $\sigma_{m,corr}$ below 35 km s^{-1}, which we regard as the lower limit to which we trust measurements of the stellar σ in individual spaxels. Prior to performing our beam-smearing correction, all measured σ_{mean} values are larger than 40 km s^{-1}; thus, $\sigma_{m,corr}$ values below 35 km s^{-1} are entirely a result of our beam-smearing correction.

We note that rotation curves may also be affected by beam smearing, in particular, the velocity gradient in the central regions. Our V_c measure is largely constrained by the asymptotic velocities at large radii and thus will be minimally affected by beam smearing (if at all). We deem the σ_{mean} correction described here necessary, however, as this is a flux-weighted quantity, and is biased towards the central regions where beam-smearing effects are at a maximum.

This paper has been typeset from a TEX/LATEX file prepared by the author.